SLAC-PUB-2233
November 1978
(T/E)

PRODUCTION AND DECAY ANGULAR DISTRIBUTIONS OF THE Y*(1385) IN THE LINE-REVERSED REACTIONS: $\pi^+p \to K^+Y^*(1385)$ AND $K^-p \to \pi^-Y^*(1385)$ AT 11.5 GeV/c[†]

C. V. Cautis, J. Ballam, J. Bouchez,[(a)] J. T. Carroll, G. B. Chadwick, V. Chaloupka, R. C. Field, D. R. Freytag, R. A. Lewis,[(b)] M.-N. Minard,[(c)] K. C. Moffeit, and R. A. Stevens[(a)]

Stanford Linear Accelerator Center, Stanford University
Stanford, California 94305

Abstract: We have measured in a single experimental setup, the differential cross sections and decay angular distributions of the Y*(1385) produced in the two line-reversed reactions: $\pi^+p \to K^+Y^{*+}(1385)$ (279 ev/μb) and $K^-p \to \pi^-Y^{*+}(1385)$ (190 ev/μb) at 11.5 GeV/c. The data have been derived from a triggered bubble chamber experiment using the SLAC Hybrid Facility. We find the differential cross sections and Y* polarizations for the two reactions to be in agreement with exchange degeneracy predictions, if kinematic differences are taken into account. The Stodolsky-Sakurai and additive quark model predictions are in agreement with the main features of the decay angular distributions of the Y*(1385), except for small violations at low momentum transfer, which can be associated with a finite helicity non-flip contribution in the forward direction.

(Submitted to Nuclear Physics)

---

† Work Supported by the Department of Energy, EY-76-C-03-0515

(a) Present address: DPhPE, CEN-Saclay, BP No. 2, F-91190, Gif-Sur-Yvette FRANCE

(b) Present address: Physics Department, Michigan State University, East Lansing, Michigan 48824, USA

(c) Present address: Laboratoire d'Annecy de Physique des Particules 74019-Annecy le Vieux, B.P. 909 FRANCE

1. INTRODUCTION

We present results in this paper from a model independent analysis of Y*(1385) production in the line-reversed reactions:

$$\pi^+ p \to K^+ Y^{*+}(1385) \quad (1)$$

$$K^- p \to \pi^- Y^{*+}(1385) \quad (2)$$

at 11.5 GeV/c incoming momentum. In a Regge picture, the two reactions are expected to be dominated asymptotically by the exchange of the same two Reggeons: the vector K*(890) and tensor K**(1420). Exchange Degeneracy (EXD) of these trajectories implies equal cross sections for reactions (1) and (2) at the same value of the four-momentum transfer, t [1]. The spin structure of the Y*(1385) is predicted by both exchange degenerate Regge poles and the additive quark model. Our experiment was designed to test these predictions.

Previous measurements of reactions (1) and (2) have mostly resulted from experiments done by different groups using different techniques [2-4], thus making comparisons difficult to interpret. The present experiment is the first one to measure, in a single detector, the complete decay angular distribution of the Y*(1385) for both reactions (1) and (2). We also measure the differential cross sections of the two reactions with a minimum of systematic differences between them. This paper is part of a continuing study of line-reversed hypercharge exchange reactions [5].

In the next section we give a description of the experimental technique, and in section 3 we describe the method used in extracting production amplitudes. The results are presented and discussed in terms of Regge phenomenology and the additive quark model in sections 4, 5, and 6. Our conclusions are summarized in section 7.

2. EXPERIMENTAL TECHNIQUE

The experiment was conducted at the SLAC Hybrid Facility (SHF) [6], exposed to 11.5 GeV/c π^+ and rf-separated K^- beams. The detector consists of the SLAC 1 m rapid cycling bubble chamber triggered by data from upstream and downstream electronic counters. The electronic data was processed online by a Data General NOVA 840 mini-computer. The bubble chamber was operated during the experiment at rates of up to 15 Hertz.

The facility combines the bubble chamber features of 4π detection, excellent tracking efficiency and mass identification of slow particles, with the advantages of a large acceptance electronic system giving good momentum resolution and mass identification for fast forward particles. The setup is shown in fig. 1.

The incident beam is measured in two Proportional Wire Chamber (PWC) stations, P1 and P2, two scintillation counters, S1 and S2, and an atmospheric pressure Čerenkov counter. Each beam PWC consists of two orthogonal wire planes.

The downstream system comprises three PWC stations, P3, P4, and P5, located in the fringe field of the bubble chamber magnet, a large aperture Čerenkov counter, C2, and a scintillation hodoscope, S3. Each downstream PWC station consists of three wire planes with angles of 0^o, 36^o and 90^o to the horizontal. At the time this experiment was run, the Čerenkov counter contained ten mirrors and phototubes, which allowed a 3 m path-length of radiator gas, and was operated with Freon 12 and Nitrogen fillings at various pressures. The elements of the hodoscope were mounted just outside the Čerenkov counter matching the ten mirrors inside. For the K^- run, a pair of hodoscopes, S4 and S5, mounted behind 1 m of iron and with

another 10 cm of iron between them, was used to veto muons from K^- decays in flight.

The electronic fast trigger for reactions 1 (2) was given by an incoming π^+ (K^-) and a fast forward K^+ (π^-) as defined by pulse height analysis of the upstream and downstream Čerenkov counters. Referring to fig. 1, the fast trigger was $S1 \cdot C1 \cdot S2 \cdot \overline{C2} \cdot S3$ for reaction (1), and $S1 \cdot \overline{C1} \cdot S2 \cdot C2$ for reaction (2). For the π^+ run, the trigger included protons as well as kaons.

The fast trigger initiates the transfer of the data to the online computer. Since it takes three milliseconds for the bubbles in the hydrogen to grow large enough to be photographed, the triggering algorithm has time to examine up to two fast triggers from the same pulse before deciding whether or not to flash the lights and take the picture.

The software decision was based on the following logic:

- The position of the incoming beam was defined by the upstream PWC stations.
- Downstream hits caused by non-interacting beam tracks were eliminated by projecting the incoming track into the downstream system using nominal values for the angles and momentum of the beam.
- The vertex coordinate along the beam direction was determined by intersecting the beam track with the downstream track in the non-bending plane. Combinations of hits giving vertices outside the fiducial volume were rejected.
- The momentum of the outgoing track was determined using the bending plane projections of those hits used to determine the vertex. The online momentum resolution was $\simeq$ 10% at 10 GeV/c. Tracks with momentum below the cutoff value were rejected.

- The pulse height from the downstream Čerenkov counter was required to be consistent with the mass assumed for the triggering particle and the measured momentum. Because of the long radiator path-length signals from kaons and pions could be separated even when both were above threshold.
- For the K^- run, the muon hodoscope was examined for corresponding hits in S4 and S5 to eliminate triggers from K^- decays.

This procedure allowed a substantial reduction in the number of pictures taken over an untriggered bubble chamber experiment (see table I). The experimental setup and the operating characteristics of the facility are discussed in detail in ref. [6].

The film was scanned for all events with a visible strange particle decay and the vertex was digitized. The events were measured in three views on precision measuring tables and reconstructed by our geometry program [7]. Tracks passing through the downstream system were constrained to fit the PWC data. The effect of this hybridization of fast forward tracks is illustrated in fig. 2 where the momentum resolution of tracks measured in the bubble chamber can be compared to the momentum resolution of the same tracks after requiring a complete fit to the bubble chamber measurements and the PWC data. The momentum resolution of hybrid tracks is $\simeq$ 1.5% at 10 GeV/c.

Events belonging to processes (1) and (2) were selected from the fully constrained reactions:

$$\pi^+ p \rightarrow K^+ \pi^+ \Lambda \qquad (3)$$

$$K^- p \rightarrow \pi^- \pi^+ \Lambda \qquad (4)$$

The selected events were required to have the fast forward track reconstructed in the downstream system and to give a seven constraint, two vertex, kinematic fit to reactions (3) or (4) with $\chi^2_{7c} < 35$. The distribution of missing mass squared for events satisfying these criteria is shown in fig. 3.

Less than 3% of the events have a missing mass above the $1\pi^0$ threshold, indicating that we have selected a clean sample of fully constrained events. We have also examined the missing mass distributions of events associated with a visible Λ decay in the chamber which fail the fits to reactions (3) or (4). From these distributions we estimate that the fraction of events lost from reactions (3) or (4), because they failed the kinematic fits, is less than 2.5%.

We have determined the sensitivities of the π^+ and K^- exposures from measurements of the incoming flux corrected for various inefficiencies. The most important losses and their errors are given in table II.

The fast electronics loss was estimated from the intensity of the incoming beam. For the π^+ exposure it also includes the loss of triggers caused by pion pile-up in the downstream Čerenkov counter.

The inefficiency of the downstream system comes from the proportional chambers and the Čerenkov counter. PWC inefficiencies affecting the triggering algorithm were calculated by an offline track reconstruction program. This used raw PWC data which was recorded whether or not a picture was taken. Because of the dead time effect, the PWCs are less efficient in the beam region as illustrated in fig. 4. Čerenkov inefficiencies were estimated from pulse-height distributions and the values of the trigger cuts.

The interaction probabilities of the incident and outgoing particles were calculated using the pion and kaon cross sections for the various materials in the beam.

The decay probability of the outgoing kaon depends on its momentum. Therefore, the events in the π^+ sample were weighted to correct for this loss. The t-dependence of the K^+ decay probability is shown in fig. 4. In the K^- exposure, the flux was corrected for the incoming K^- and outgoing π^- decay probabilities.

The muon content of the π^+ beam was known from an independent measurement. The hadron punch-through was estimated by running the π^+ beam into the muon filter, counting the number of hits in the hodoscope and correcting for the known muon contamination.

The algorithm losses were estimated with a Monte Carlo method. A weight was applied to each event to correct for the loss of events at small momentum transfer caused by the "beam veto" feature of the algorithm (see fig. 4).

Typical bubble chamber data handling losses, and losses caused by Λ decays outside the fiducial volume were estimated by standard procedures. Losses caused by the finite efficiency of the hybridization program to match bubble chamber tracks to PWC data, were estimated by running the entire sample of events through two independent hybridization programs and comparing the results.

In fig. 4, we show the momentum transfer dependence of the detection efficiency of the facility averaged over the mass of the Y*(1385). The geometric acceptance of the downstream system is 100% for Y*(1385) below 1 GeV^2 momentum transfer.

All cross sections were corrected for the losses described above. The uncertainties inherent in these corrections yield a systematic error of ± 10% in the normalization. However, the maximum relative uncertainty between the π^+ and K^- exposures is only 9%.

In addition, we find small losses in the Λ sample, which affect some of the angular distributions. Such losses come from asymmetric vees in which one of the tracks (mostly π^-) is too short to be measured properly and vees with a small opening angle which are misidentified as γ conversions. These losses amount to $\lesssim 3\%$ and have been taken into account when fitting the angular distributions.

The sample of events used in the present analysis is described in table I. The Dalitz and Chew-Low plots for the three particle final states are shown in figs. 5 and 6. It is apparent from fig. 5 that although there is abundant $\rho^0\Lambda$ production in reaction (4), this process has negligible overlap with the Y*(1385). The distributions of $\Lambda\pi^+$ invariant masses are shown in fig. 7. The data show a strong Y*(1385) peak over a background level less than 10% of the signal. The mass resolution in the Y*(1385) region is 8 MeV/c^2 (FWHM).

3. METHOD OF ANALYSIS

We have made a model independent analysis of Y*(1385) production in reactions (3) and (4). The six independent variables which we choose to describe the four-particle final state are: t, the square of the four-momentum transfer from the beam to the fast forward particle (K^+ or π^-), $m_{\Lambda\pi^+}$, the invariant mass of the $\Lambda\pi^+$ system and Ω, a set of four polar angles describing the cascade decay: $Y^* \to \Lambda\pi^+$, $\Lambda \to p\pi^-$, as defined below.

For a fixed incoming energy and fixed region of momentum transfer,

we write the probability density function as an incoherent sum:

$$\omega = C_1 \cdot BW_{1385}(m_{\Lambda\pi^+}) \cdot W(\Omega) + C_2 \cdot BW_2 + C_3 \cdot BW_3 + C_4 \qquad (5)$$

where C_i are constants, BW_i are Breit-Wigner propagators and $W(\Omega)$ is the complete decay angular distribution of the Y*(1385). The terms in C_2 and C_3 were included to describe the $m_{\Lambda\pi} = 1700$ GeV/c^2 region. For the Y*(1385), we used a p-wave Breit-Wigner [8]:

$$BW(m) = \frac{m}{p} \frac{\Gamma}{\left(m^2 - m_0^2\right)^2 + m_0^2\Gamma^2}$$

$$\Gamma = \Gamma_0 \left(\frac{p}{p_0}\right)^{2\ell+1} \cdot \frac{a^2+p_0^2}{a^2+p^2} \qquad (6)$$

where m_0 and Γ_0 are the mass and width of the Y*(1385), p is the momentum of the Λ in the $\Lambda\pi^+$ rest frame, ℓ is the orbital angular momentum of the $\Lambda\pi^+$ system ($\ell = 1$ for the Y*(1385)) and a is constant (we used $a = .1$ GeV/c).* The decay angular distribution of the Y*was measured in the transversity frame defined with the z-axis along the normal to the production plane: $\hat{z} = \hat{B} \times \hat{M}$ where $\hat{B}$ is the direction of the beam and $\hat{M}$ is the direction of the system recoiling against the $\Lambda\pi^+$. The y axis was taken along the direction of the $\Lambda\pi^+$ system in the overall center-of-mass frame. The Λ decay was measured in the frame with $\hat{z}' = \hat{\Lambda}$ in the Y* rest frame and

* Jackson [8] suggests $a \sim m_\pi$ for the Δ^{++} resonance. We found the fit insensitive to the exact value of a, for $a < .2$ GeV. We used the value $a = .1$ GeV, the same as in ref. [3].

$\hat{y}' = \hat{z} \times \hat{z}'$. With this choice of axes, the decay angular distribution of the $Y^{*}_{\pm}(1385)$ can be written as [3,9]:

$$W(\Omega) = \frac{1}{2\pi} \sum_{\substack{\lambda\ \mu \\ \lambda'\mu'}} D^{*3/2}_{\lambda\mu}(\phi,\theta) \cdot D^{3/2}_{\lambda'\mu'}(\phi,\theta) \cdot M_{\mu\mu'}(\theta',\phi') \cdot \rho_{\lambda\lambda'}$$

$$M_{\pm\frac{1}{2}\pm\frac{1}{2}} = \frac{1}{4\pi}(1 \pm \alpha \cos\theta') \tag{7}$$

$$M_{\pm\frac{1}{2}\mp\frac{1}{2}} = \frac{\alpha}{4\pi} \sin\theta' \cdot e^{\pm i\phi'}$$

where λ is the transversity of the $Y^{*}(1385)$, μ is the helicity of the Λ and α is the Λ decay asymmetry parameter ($\alpha = .647$). The spin density matrix $\rho_{\lambda\lambda'}$ can be written in terms of transversity amplitudes $T_{\mu\nu}$ as:

$$\rho_{\lambda\lambda'} = \sum_{\nu} T_{\lambda\nu} \cdot T^{*}_{\lambda'\nu} \tag{8}$$

where ν is the transversity of the incoming proton. This shows that the maximum rank of ρ is two.

Parity conservation in the production process requires for the $Y^{*}(1385)$:

$$T_{\mu\nu} = (-1)^{\mu-\nu}\ T_{\mu\nu} \tag{9}$$

This leaves four non-zero transversity amplitudes:

$$T_{3/2\ -1/2},\ T_{-1/2\ -1/2},\ T_{1/2\ 1/2},\ T_{-3/2\ 1/2} \tag{10}$$

The real and imaginary parts of the transversity amplitudes are parameters in the fit. This parametrization insures the positivity and proper rank of ρ. By relaxing the rank condition, we have verified that the data does not require a rank greater than two even when integrated over large intervals of momentum transfer.

Measurement of the weak, parity violating decay of the Λ allows the determination of the complete Y*(1385) spin density matrix. In the transversity frame, because of relation (9), we can determine the absolute values of the four amplitudes and two of the relative phases. The overall phase and the phase between proton spin "up" and "down" cannot be measured in this experiment. For convenience, the unknown phases were arbitrarily fixed by imposing Im $T_{1/2\ 1/2}$ = Im $T_{-1/2\ -1/2}$ = 0.

The one dimensional distributions of the four angles describing the full decay of the Y*(1385) in the transversity frame are obtained by integrating the decay angular distribution [7] over three of the four angles:

$$W(\cos\theta) = \frac{3}{4}\sin^2\theta\,(T^2_{3\ -1} + T^2_{-3\ 1}) + \frac{1}{4}(1 + 3\cos^2\theta)\,(T^2_{1\ 1} + T^2_{-1\ -1})$$

$$W(\phi) = \frac{1}{2\pi} - \frac{2}{\pi\sqrt{3}}\left\{T_{3\ -1}\cdot T_{-1\ 1}\cos(2\phi + \psi_{3\ -1}) + T_{-3\ 1}\cdot T_{1\ 1}\cos(2\phi + \psi_{1\ -3})\right\}$$

$$W(\cos\theta') = \frac{1}{2} \qquad (11)$$

$$W(\phi') = \frac{1}{2\pi} - \frac{\alpha\pi}{32}\left\{\frac{9}{8}(T^2_{3\ -1} - T^2_{-3\ 1}) + \frac{5}{8}(T^2_{1\ 1} - T^2_{-1\ -1})\right\}\cos\phi'$$

where T_{ij} are the absolute values of the amplitudes and ψ_{ij} are phase differences between the corresponding amplitudes. Here and below, the integer indices in T_{ik} represent the corresponding transversities multiplied by two. These distributions were not used in the analysis, but are useful in interpreting the data (see fig. 8).

The transversity frame is related to the s-channel helicity frame (i.e., z-axis along Y*) by a rotation R = ($\pi/2$, $\pi/2$, $\pi/2$). There are eight helicity amplitudes constrained by four linear relations:

$$H_{\lambda_1\lambda_2} = \eta(-1)^{J_1 - J_2 - \lambda_1 + \lambda_2} \cdot H_{-\lambda_1 -\lambda_2} \tag{12}$$

where η is the product of intrinsic parities of all particles in the interaction. This leaves four independent helicity amplitudes:

$$H_{\lambda_1\lambda_2} = \sum_{\tau_1\tau_2} T_{\tau_1\tau_2} \cdot (i)^{\tau_1 - \tau_2 + \lambda_1 - \lambda_2} \cdot d^{3/2}_{\tau_1\lambda_1}(\pi/2) \cdot d^{1/2}_{\tau_2\lambda_2}(\pi/2) \tag{13}$$

where τ are transversities and λ are helicities.

To facilitate the discussion of results in section 5, we give here the explicit relations:

$$\begin{aligned}
H_{3\ 1} &= H_{-3\ -1} = \tfrac{i}{4}\,(-T_{3\ -1} + \sqrt{3}\,T_{1\ 1} + \sqrt{3}\,T_{-1\ -1} - T_{-3\ 1}) \\
H_{1\ 1} &= -H_{-1\ -1} = \tfrac{1}{4}\,(\sqrt{3}\,T_{3\ -1} - T_{1\ 1} + T_{-1\ -1} - \sqrt{3}\,T_{-3\ 1}) \\
H_{-1\ 1} &= H_{1\ -1} = \tfrac{i}{4}\,(\sqrt{3}\,T_{3\ -1} + T_{1\ 1} + T_{-1\ -1} + \sqrt{3}\,T_{-3\ 1}) \\
H_{-3\ 1} &= -H_{3\ -1} = \tfrac{1}{4}\,(-T_{3\ -1} - \sqrt{3}\,T_{1\ 1} + \sqrt{3}\,T_{-1\ -1} + T_{-3\ 1})
\end{aligned} \tag{14}$$

The inverse transformation is:

$$
\begin{aligned}
T_{3\ -1} &= \frac{1}{2}\ \{\ (\sqrt{3}\ H_{1\ 1} - H_{-3\ 1}) - i(\sqrt{3}\ H_{-1\ 1} - H_{3\ 1})\ \} \\
T_{1\ 1} &= \frac{1}{2}\ \{-(H_{1\ 1} + \sqrt{3}\ H_{-3\ 1}) - i(H_{-1\ 1} + \sqrt{3}\ H_{3\ 1})\ \} \\
T_{-1\ -1} &= \frac{1}{2}\ \{\ (H_{1\ 1} + \sqrt{3}\ H_{-3\ 1}) - i(H_{-1\ 1} + \sqrt{3}\ H_{3\ 1})\ \} \\
T_{-3\ 1} &= \frac{1}{2}\ \{-(\sqrt{3}\ H_{1\ 1} - H_{-3\ 1}) - i(\sqrt{3}\ H_{-1\ 1} - H_{3\ 1})\ \}
\end{aligned}
\tag{15}
$$

One can see from relation (14), that in the absence of the relative phase between transversity amplitudes, one cannot obtain individual helicity amplitudes. However, one can measure certain linear combinations of helicity amplitudes (so-called "mixed amplitudes") or the density matrix elements. We calculated the density matrix in the helicity frame, using fitted transversity amplitudes according to the rotation:

$$
\rho^{H}_{\lambda\lambda'} = \sum_{\nu\nu'} D^{3/2}_{\lambda\nu}\ (-R) \cdot D^{3/2}_{\nu'\lambda'}(R) \cdot \rho^{T}_{\nu\nu'} \tag{16}
$$

Where R = (π/2, π/2, π/2). The parity relations (12) insure that ρ^{H} is symmetric about the second diagonal.

We used the extended maximum likelihood method [10] to estimate from the data the total amount of Y*(1385) production and the contribution of the four transversity amplitudes as functions of momentum transfer. We write the log-likelihood function as:

$$
\log L = \sum_{i=1}^{N} \log\ \omega_i - \int \omega\ d\tau \tag{17}
$$

where N is the total number of events in the sample, and the integral is performed over the same region of phase-space as the one used to select the experimental sample. This method insures the normalization of each

amplitude over the phase-space region selected for the fit. All cuts imposed on the experimental sample, in order to eliminate the biased regions, are taken into account in calculating the integral.

The maximization of the log-likelihood function was done using the program OPTIME [11]. After each fit we have plotted the result of the fit on top of different experimental distributions and found good agreement with the data (see fig. 8). We have also verified that the results of the fits were not dependent on exact values chosen for the cuts on the data or the t intervals. The differential cross sections were alternatively estimated by a simple background subtraction, and the transversity amplitudes were also extracted by the method of moments. The different methods agreed within one standard deviation with the maximum likelihood analysis.

4. DIFFERENTIAL CROSS SECTIONS

We measured total and differential cross sections from fits in the region $m_{\Lambda\pi^+} < 2$ GeV/c^2. To obtain a good description of the mass spectrum up to 2 GeV/c^2, we tried several parametrizations for the background. We obtained the best fit with a p-wave Breit-Wigner [8] for the Y*(1385), and two simple Breit-Wigner functions in the $m_{\Lambda\pi^+} \sim 1.7$ GeV/c^2 region, plus a constant phase-space term.

The results for the Y*(1385) did not depend on the parametrization used for the background. The parameters of the Y*(1385) and the high-mass enhancements were determined from fits in the region $m_{\Lambda\pi^+} < 2$ GeV/c^2 and $-t < 1$ GeV^2. We found the mass and width of the Y*(1385) to be consistent within errors in the π^+ and K^- reactions. In the final fits we used the average values:

$m_0 = (1.381 \pm .002)$ GeV/c^2 and $\Gamma = (.030 \pm .004)$ GeV/c^2. (See fig. 7.)

With the mass and width of the Y*(1385) fixed, we have measured the differential cross sections by fitting the amount of resonance production in several t-intervals up to $-t = 1$ GeV^2. The cross sections for reactions (1) and (2) have been corrected for the $Y^*(1385) \to \Lambda\pi$ and $\Lambda \to p\pi^-$ decay branching ratios (0.88 and 0.642, respectively). The results are shown in fig. 9 and the corresponding cross sections are given in table III.

The two differential cross sections show a turnover in the forward direction suggesting that the Y* vertex is helicity flip dominated. The slopes of the two distributions are similar, but there are significant differences between cross sections at small $|t|$. Most of the difference between the π^+ and K^- induced cross sections is of kinematic origin: Angular momentum conservation forces the helicity flip dominated cross section to go to zero at $\langle t_{min} \rangle = -.012$ GeV^2 in reaction (1) and at $\langle t_{min} \rangle = +.011$ GeV^2 in reaction (2), thus yielding different cross sections at small $|t|$.

To describe this effect quantitatively, we did minimum χ^2 fits to the differential cross sections using the function:

$$\frac{d\sigma}{dt} = A_1 e^{b_1 t} - A_2 (t-t_{min}) e^{b_2 t} \qquad (18)$$

where A_1 and A_2 approximate the helicity non-flip and flip contritutions, respectively. After finding the best fit to the shape of the distribution, we normalized A_1 and A_2 so that the fit and the data would cover the same area. This renormalization changed the results of the fits by $\simeq 2.5\%$.

The slopes b_1 and b_2 were determined by the fit to be equal to each other within errors, and equal between the π^+ and K^- cross sections. For the final fits we fixed all slopes to the mean value $b = (7.0 \pm .4)$ GeV^{-2}.

The fits give a good description of the data as shown in fig. 9. In particular, the turnover in the forward direction is well described by eq. (18) supporting thus the kinematic origin of the difference in cross sections at low $|t|$ between reactions (1) and (2).

The values obtained for the parameters A_1 and A_2, were as follows: $A_1 = (9 \pm 4)$ $\mu b/GeV^2$, $A_2 = (297 \pm 40)$ $\mu b/GeV^3$ for reaction (1) and $A_1 = (11 \pm 4)$ $\mu b/GeV^2$, $A_2 = (350 \pm 46)$ $\mu b/GeV^3$ for reaction (2). (The errors include the systematic uncertainty.) These values are consistent within errors with earlier estimates [5] which did not explicitly normalize the fit to the experimental distribution.

One can approximate, in general, the phase difference between the vector and tensor amplitudes in line-reversed reactions as (1) and (2) in the form [12]:

$$\langle \cos \phi_{VT} \rangle = \frac{\left(\frac{d\sigma}{dt}\right)_{K^-} - \left(\frac{d\sigma}{dt}\right)_{\pi^+}}{\left(\frac{d\sigma}{dt}\right)_{K^-} + \left(\frac{d\sigma}{dt}\right)_{\pi^+}} \qquad (19)$$

For the helicity flip dominated processes (1) and (2), this calculation is distorted by kinematic effects.

To eliminate kinematic factors, we have calculated eq. (19) using the fitted values of A_2 instead of cross sections. If the only difference between the π^+ and K^- cross sections were due to the difference in t_{min}, exchange degeneracy would predict this value to be zero. We obtained $\langle \cos \phi_{VT} \rangle = .08 \pm .08$ in good agreement with EXD predictions.

The integrated cross section for reaction (1) is $\simeq$ 30% smaller than that for reaction (2), but our analysis indicates that half of the difference is due to the t_{min} effect. The remaining discrepancy is within the limits of systematic uncertainties in this experiment. We

conclude, therefore, that the equal cross section criterion is not a good test of exchange degeneracy in helicity-flip dominated processes. This conclusion is based on the shapes of the differential cross sections, reinforced by the results of fits with the function (18). The physics content of the parametrization (18) was independently confirmed by the results of the transversity amplitude analysis as described in the next section.

5. AMPLITUDE ANALYSIS

For the amplitude analysis, we made fits in the mass range $m_{\Lambda\pi^+} < 1.55$ GeV/c^2. In this region an isotropic phase-space is adequate as background ($C_2 = C_3 = 0$ in eq.(5)).

The absolute values of the four transversity amplitudes are shown as functions of t in fig. 10, and the real and imaginary parts of all amplitudes are listed in tables IV and V. Density matrix elements in the helicity frame are shown in fig. 11 and in tables VI and VII.

If the two reactions (1) and (2) are produced by the exchange of two degenerate Regge poles, all helicity amplitudes would have the same phase. One would expect then, from eq. (15), that the transversity matrices for each of reactions (1) and (2) separately would be symmetric about the second diagonal.

The additive quark model reinforces the up/down symmetry prediction. Assuming that the interaction occurs only through a single quark-quark scattering, amplitudes corresponding to changes of more than one unit of angular momentum along any axis are forbidden. For reactions (1) and (2), this implies (class A predictions [13]): $T_{\pm 3/2\ \mp 1/2} = 0$, $T_{1/2\ 1/2} = T_{-1/2\ -1/2}$. These predictions can be inferred from eq. (15). The resulting decay

angular distribution is the same as that expected for a $M1 \rightarrow p_{3/2}$ transition based on vector-meson photon analogy [14].

These predictions are indicated as dashed lines in figs. 10 and 11. They are in agreement with the main features of the data for both reactions (1) and (2).

The absolute values of the quark model forbidden amplitudes $T_{\pm 3/2\ \mp 1/2}$, which are positive definite, are within one standard deviation from zero for $-t > .1$ GeV^2. The only significant non-zero double-flip values are at small t, and are similar to those observed at 4.2 GeV/c in $\bar{K}p$ interactions [3]. This effect may be associated with a finite helicity non-flip contribution to the Y*(1385) vertex. At $t=t_{min}$, all helicity flip amplitudes go rigorously to zero. Any remaining non-flip contribution forces the transversity amplitudes to the values (see eq. (15)):

$$\left|T_{\pm 3/2\ \mp 1/2}\right| = \sqrt{\frac{3}{8}}\ ; \quad \left|T_{\pm 1/2\ \pm 1/2}\right| = \sqrt{\frac{1}{8}} \qquad (20)$$

in the forward direction. The trend in our data is in qualitative agreement with these values. In quark model language the non-zero values of $T_{3/2\ -1/2}$ and $T_{-3/2\ 1/2}$ imply double quark scattering which is expected to contribute at small angles [15].

Additional confirmation of helicity non-flip contribution to the Y*(1385) vertex comes from the study of the differential cross section and the spin density matrix elements in the helicity frame. Fits to the Y*(1385) differential cross sections indicate a 16-20% helicity non-flip contribution. The s-channel helicity frame matrix elements shown in fig. 11 (and in tables VI and VII) are also consistent with an increased non-flip contribution in the forward direction as seen in the larger value of ρ_{11}

at low t values. We have verified that the effects observed in the forward direction in the transversity amplitudes and in the helicity density matrix elements agree in magnitude and t-dependence with the helicity non-flip contribution estimated from the differential cross sections.

The double-flip amplitudes which show the strongest deviation from zero are the $T_{3/2\ -1/2}$ in reaction (1) and $T_{-3/2\ 1/2}$ in reaction (2). This reflection symmetry for the line-reversed reactions is in agreement with weak EXD predictions.

6. DISCUSSION OF RESULTS

Previous measurements of reactions (1) and (2) have found a large difference between the π^+ and K^- cross sections [2, 3, 4] ($\sigma_{K^-} \gtrsim 2\ \sigma_{\pi^+}$) implying strong violations of exchange degeneracy. In contrast, Σ^+ production in the helicity non-flip dominated processes:

$$\pi^+ p \to K^+ \Sigma^+ \tag{21}$$

$$K^- p \to \pi^- \Sigma^+ \tag{22}$$

has been shown to be in approximate agreement with EXD predictions [5, 16] in our energy range. The cross sections are nearly equal for $-t < .4$ GeV^2 and the Σ polarization has the same magnitude, but opposite sign, in the two line-reversed reactions suggesting interference between two Regge amplitudes with degenerate trajectories but opposite signatures. Reactions (21) and (22) are expected to be dominated by vector and tensor exchange similar to Y*(1385) production in reactions (1) and (2).

From our data we find that the helicity flip dominated processes (1) and (2) are in agreement with the predictions of degenerate Regge poles exchange, contrary to conclusions of previous experiments. To understand

this difference we will review some of the characteristic features of this experiment.

Our experiment was done at a higher energy than most previous experiments, and we would expect the difference in cross sections between reactions (1) and (2) to decrease with energy. We also measured both reactions in a single experimental setup, thus minimizing systematic differences between the two exposures.

In the hybrid facility, we measure the vertex, the incoming beam track, and all outgoing particles for reactions (3) and (4). The events are fully constrained kinematically, giving good mass resolution (e.g., 8 MeV/c^2 at $\simeq$ 1.4 GeV/c^2), and very small background under the Y*(1385) (see fig. 7).

The largest systematic error in this experiment comes from the uncertainty in the overall normalization, i.e., $\pm$ 10%. We have done an absolute determination of the sensitivity, rather than normalize to a previously measured cross section.

In figs. 12, 13, and 14, we compare our cross sections for reactions (1), (2), (21), and (22) to those of other experiments. We have included in these plots preliminary results from the same apparatus obtained by the Imperial College group [17] as well as preliminary results at 70 GeV/c [18] obtained at FNAL. It is apparent from all three figures that our cross sections are in agreement with most other experiments in the same energy range.

We would like to point out that the energy dependence of reactions (21) and (22) is consistent with degenerate vector and tensor K* exchange, while reaction (1) has a shallower energy dependence at t = -.10 GeV^2, but not at t = -.25 GeV^2. This suggests that the contribution of the helicity non-flip amplitude at the Y*(1385) vertex, which is quark model

forbidden, has a weaker energy dependence than the dominant helicity flip term so that the cross section drops off with energy slower at small $|t|$ than at larger $|t|$ values. However, this observation depends critically on the results at 70 GeV/c which are still preliminary [18]. The cross sections for reaction (2) are not inconsistent with the same energy dependence as reaction (1) if the variation of t_{min} with energy is taken into account.

7. CONCLUSIONS

We have measured the differential cross sections and full decay angular distributions of the Y*(1385) in the line-reversed reactions (1) and (2). In contrast to previous experiments, we find the predictions of degenerate vector and tensor K* exchange in agreement with the data, within the limits of systematic uncertainties. We would expect the agreement to be even better at Fermilab energies where kinematic effects would also become less important.

The results of the Y*(1385) amplitude analysis are consistent with the results of similar studies at much lower energies [3, 9]. The contribution of the quark model forbidden helicity non-flip amplitude in the forward direction as estimated from the differential cross section, can be associated with the double-quark scattering effects observed in the amplitude analysis.

ACKNOWLEDGMENTS

We want to thank the operating crews of the beam and of the 40-in bubble chamber, as well as the scanning and measuring group under the supervision of Marie LaBelle for their efforts on this experiment. We are also indebted to our colleagues from Imperial College, Purdue and Toronto Universities for helping with the data taking. The contribution of Peter Dornan, Andy White and Geoff Hall from Imperial College, who have developed the online algorithm, is gratefully acknowledged.

References

[1] F. J. Gilman, Phys. Lett. 29B, (1969) 673, R. C. Arnold, Phys. Rev. 153, (1967) 1506, K. W. Lai and J. Louie, Nucl. Phys. B19, (1970) 205.

[2] J. Bartsch et al., Nuovo Cimento 43A, (1966) 1010, D. C. Colley et al., Nuovo Cimento 53A, (1968) 522, J. Mott et al., Phys. Rev. 177, (1969) 1966, M. Aderholz et al., Nucl. Phys. B7, (1968) 111, and ibid. B11, (1969) 259, W. A. Cooper et al., Nucl. Phys. B23, (1970) 605, P. Girtler et al., Nucl. Phys. B99, (1975) 13, A. Bashian et al., Phys. Rev. D 4, (1971) 2667, M. Aguilar-Benitez et al., Phys. Rev. D 6, (1972) 29, D. Birnbaum et al., Phys. Lett. 31B, (1970) 484, B. Chaurand et al., Nucl. Phys. B117, (1976) 1.

[3] S. O. Holmgren et al., Nucl. Phys. B119, (1977) 261.

[4] A. Berglund et al., Phys. Lett. 60B, (1975) 117, and A. Berglund A Study of the Line-Reversed Hypercharge Exchange Reactions $\pi^+ p \to K^+\Sigma^+$ and $K^- p \to \pi^-\Sigma^+$ at 7.0 and 10.1 GeV/c, Ph.D. Thesis, University of Stockholm (1978).

[5] J. Ballam et al., Phys. Rev. Lett. 41, (1978) 676.

[6] G. B. Bowden et al., Nucl. Instr. and Meth. 138, (1976) 75, J. Ballam and R. Watt, Ann. Rev. Nucl. Sci. 27, (1977) 75, R. C. Field, SHF Memo 67, Stanford Linear Accelerator Center internal publication, Group BC, (1977).

[7] F. T. Solmitz et al., Three View Geometry Program, Alvarez Group Programming Note P-117, Berkeley internal publication (1966).

[8] J. D. Jackson, Nuovo Cimento 34, (1964) 1644.

[9] Aguilar-Benitez et al., Phys. Rev. Lett. 29, (1972) 749.

[10] J. Orear, Notes on Statistics for Physicists, University of California Radiation Laboratory, Berkeley preprint UCRL-8417 (1958).

[11] P. H. Eberhard and W. D. Koellner, Comp. Phys. Comm. 3, (1972) 296, and ibid. 5, (1973) 163.

[12] A. C. Irving and R. P. Worden, Phys. Rep. 34C, (1977) 117.

[13] A. Bialas and K. Zalewski, Nucl. Phys. B6, (1968) 449.

[14] L. Stodolsky and J. J. Sakurai, Phys. Rev. Lett., 11, (1963) 90.

[15] F. Wagner, The Additive Quark Model for Δ and Y* Reactions, Max-Plank-Institute report MPI-PAE/PTh 19/76 (1976), Invited Talk at the XI Recontre de Moriond, (1976).

[16] A. Berglund et al., Phys. Lett. 73B, (1978) 369.

[17] P. A. Baker et al., Imperial College report IC/HENP/78/21 (1978) or Stanford Linear Accelerator Center report SLAC-PUB-2169 (1978).

[18] M. W. Arenton et al., Argonne National Laboratory report ANL-HEP-PR-78-24 (1978).

[19] G. G. G. Massaro et al., Phys. Lett. 66B, (1977) 385.

Table I - Statistics of the experiment and cross sections. The error on the cross section includes 10% systematic uncertainty.

Reaction	Pictures ($\times 10^6$)	Sensitivity † (ev/μb)	Events	Cross Section (μb)
$\pi^+ p \to K^+ Y^*(1385)$	1.2	279	936	6.5 ± .7
$K^- p \to \pi^- Y^*(1385)$	.8	190	911	9.6 ± 1.0

† The difference from an earlier estimate [5] of the sensitivity comes from a more detailed evaluation of π and K interaction probabilities in the material of the detector.

Table II - Values of typical losses used to correct the sensitivities of the two exposures.

Losses	$\pi^+ p \to K^+_{fwd}$ (%)	$K^- p \to \pi^-_{fwd}$ (%)
Fast electronics	11.5 ± 2.0	8.0 ± 2.0
Beam PWC	5.2 ± 2.0	7.2 ± 2.2
Downstream PWC	6.5 ± 2.0	6.8 ± 1.5
C_2 inefficiency	2.0 ± 1.0	1.5 ± 1.0
Interactions of incident or outgoing particle	15.5 ± 5.0	17.8 ± 5.0
Kaon decay	6.0 ± 1.0	5.2 ± 1.0
Muon contamination in the beam	8.0 ± 2.5	----------
Hadron punchthrough	----------	8.5 ± 2.5
Scanning*	3.4 ± 1.5	3.0 ± 1.5
Measuring*	2.8	2.5
Hybridization	2.4 ± 1.5	2.8 ± 1.5
Λ decay	6.7 ± 1.9	7.2 ± 1.9

* Losses refer to the topology: 2 prongs, 1 V^o.

Table III - Differential cross sections at 11.5 GeV/c incoming momentum. Only statistical errors are given.

$-t$ (GeV^2)	$\frac{d\sigma}{dt}(\pi^+ p \to K^+ Y^*(1385))$ ($\mu b/GeV^2$)	$\frac{d\sigma}{dt}(K^- p \to \pi^- Y^*(1385))$ ($\mu b/GeV^2$)
-.01, .02	----------	14.5 ± 3.5
.02, .06	11.7 ± 1.8	21.3 ± 3.0
.06, .10	16.9 ± 2.1	26.3 ± 3.0
.10, .14	23.2 ± 1.9	23.8 ± 3.1
.14, .18	16.9 ± 2.1	21.6 ± 2.9
.18, .24	13.9 ± 1.5	18.3 ± 2.1
.24, .30	12.1 ± 1.4	16.6 ± 2.0
.3 , .4	9.8 ± 1.4	11.9 ± 1.3
.4 , .5	4.4 ± .7	9.5 ± 1.2
.5 , .7	3.1 ± .4	3.5 ± .5
.7 , 1.	.77± .16	.91± .22

Table IV - Transversity amplitudes of the Y*(1385) produced in the reaction $\pi^+ p \to K^+ Y^{*+}(1385)$. The imaginary parts of T_{11} and $T_{-1\,-1}$ were arbitrarily fixed at zero.

$-t$ (GeV^2)	Re $T_{-3\,1}$	Im $T_{-3\,1}$	Re $T_{-1\,-1}$	Re $T_{1\,1}$	Re $T_{3\,-1}$	Im $T_{3\,-1}$
$-t_{min}$, .06	.21 ± .19	.39 ± .20	.38 ± .26	.81 ± .14	-.05 ± .48	.02 ± .51
.06, .12	.26 ± .12	.19 ± .13	.74 ± .10	.57 ± .12	-.06 ± .11	.12 ± .13
.12, .18	-.15 ± .13	-.00 ± .12	.68 ± .10	.70 ± .10	.09 ± .13	.14 ± .12
.18, .24	.11 ± .13	.03 ± .14	.53 ± .14	.81 ± .10	.20 ± .16	-.08 ± .17
.24, .30	.00 ± .15	.12 ± .17	.76 ± .10	.63 ± .12	.01 ± .13	.08 ± .12
.3 , .4	-.21 ± .17	-.03 ± .16	.77 ± .12	.55 ± .12	-.22 ± .16	.00 ± .14
.4 , .6	.09 ± .18	.29 ± .17	.83 ± .09	.46 ± .18	-.04 ± .14	.06 ± .12
.6 ,1.	-.01 ± .27	.28 ± .18	.76 ± .14	.55 ± .18	.02 ± .18	-.17 ± .16

Table V - Transversity amplitudes of the Y*(1385) produced in the reaction $K^- p \to \pi^- Y^{*+}(1385)$.

The imaginary parts of $T_{1\ 1}$ and $T_{-1\ -1}$ were arbitrarily fixed at zero.

$-t$ (GeV^2)	Re $T_{-3\ 1}$	Im $T_{-3\ 1}$	Re $T_{-1\ -1}$	Re $T_{1\ 1}$	Re $T_{3\ -1}$	Im $T_{3\ -1}$
$-t_{min}$, .06	-.04 ± .22	-.14 ± .19	.76 ± .10	.50 ± .14	.13 ± .13	.38 ± .14
.06, .12	-.10 ± .14	-.06 ± .12	.68 ± .09	.68 ± .10	.02 ± .16	.23 ± .13
.12, .18	-.15 ± .17	.10 ± .17	.76 ± .11	.61 ± .13	.10 ± .13	-.05 ± .12
.18, .24	-.24 ± .16	-.13 ± .16	.68 ± .12	.61 ± .12	.04 ± .13	.30 ± .14
.24, .30	-.01 ± .24	.04 ± .32	.87 ± .11	.49 ± .17	.02 ± .13	.01 ± .13
.3 , .4	.06 ± .11	.03 ± .15	.63 ± .12	.75 ± .10	.02 ± .16	.20 ± .17
.4 , .6	.08 ± .14	-.01 ± .13	.74 ± .09	.66 ± .10	-.01 ± .10	-.13 ± .11
.6 ,1.	-.10 ± .23	.11 ± .36	.77 ± .16	.59 ± .19	.12 ± .20	.18 ± .25

Table VI - Helicity density matrix elements of the Y*(1385) produced in the reaction:

$\pi^+ p \rightarrow K^+ Y^{*+}(1385)$.

$-t$ (GeV^2)	$\rho_{3\,3}$	$\rho_{1\,1}$	Re $\rho_{3\,1}$	Im $\rho_{3\,1}$	Re $\rho_{3\,-1}$	Im $\rho_{3\,-1}$	Im $\rho_{1\,-1}$	Im $\rho_{3\,-3}$
$-t_{min}$, .06	.26 ± .07	.24 ± .06	.16 ± .08	.12 ± .08	.18 ± .08	-.15 ± .08	-.22 ± .10	.11 ± .10
.06, .12	.30 ± .07	.20 ± .05	.01 ± .06	-.02 ± .06	.21 ± .06	-.01 ± .06	-.09 ± .05	-.15 ± .08
.12, .18	.38 ± .08	.12 ± .05	.05 ± .05	-.04 ± .05	.15 ± .06	.05 ± .05	.07 ± .06	.08 ± .07
.18, .24	.28 ± .08	.23 ± .08	-.01 ± .09	.09 ± .10	.19 ± .08	-.03 ± .06	-.03 ± .08	.12 ± .08
.24, .30	.37 ± .07	.14 ± .06	.07 ± .08	-.04 ± .06	.21 ± .06	-.01 ± .05	.02 ± .07	-.05 ± .06
.3 , .4	.48 ± .08	.02 ± .07	-.01 ± .05	-.05 ± .06	.19 ± .05	.01 ± .08	.01 ± .06	-.12 ± .08
.4 , .6	.35 ± .09	.15 ± .07	.09 ± .06	-.10 ± .08	.19 ± .06	-.04 ± .06	-.01 ± .07	-.18 ± .10
.6 ,1.	.34 ± .10	.16 ± .08	.01 ± .07	-.08 ± .10	.16 ± .10	-.14 ± .10	.03 ± .08	-.07 ± .08

Table VII - Helicity density matrix elements of the Y*(1385) produced in the reaction:

$K^- p \to \pi^- Y^{*+}(1385)$.

$-t$ (GeV^2)	$\rho_{3\,3}$	$\rho_{1\,1}$	Re $\rho_{3\,1}$	Im $\rho_{3\,1}$	Re $\rho_{3\,-1}$	Im $\rho_{3\,-1}$	Im $\rho_{1\,-1}$	Im $\rho_{3\,-3}$
$-t_{min}$, .06	.29 ± .08	.20 ± .06	.11 ± .06	-.07 ± .07	.11 ± .06	.18 ± .10	.14 ± .11	-.07 ± .10
.06, .12	.38 ± .07	.12 ± .06	.06 ± .07	-.01 ± .08	.17 ± .05	.10 ± .09	.05 ± .08	.03 ± .08
.12, .18	.37 ± .07	.13 ± .06	.01 ± .06	-.09 ± .08	.16 ± .05	-.05 ± .07	.09 ± .09	.01 ± .09
.18, .24	.39 ± .09	.11 ± .06	.06 ± .08	-.06 ± .09	.10 ± .08	.14 ± .10	.09 ± .12	.04 ± .12
.24, .30	.38 ± .06	.13 ± .07	.01 ± .06	-.12 ± .08	.21 ± .06	-.01 ± .08	.07 ± .09	-.16 ± .14
.3 , .4	.34 ± .08	.16 ± .08	.07 ± .07	.05 ± .06	.21 ± .05	.05 ± .07	-.02 ± .08	.03 ± .08
.4 , .6	.35 ± .08	.15 ± .07	-.05 ± .06	-.01 ± .06	.22 ± .06	-.04 ± .09	-.01 ± .09	-.06 ± .09
.6 ,1.	.34 ± .10	.16 ± .09	.10 ± .08	-.08 ± .10	.15 ± .08	.04 ± .12	.10 ± .10	-.02 ± .12

Figure Captions

Fig. 1. Layout of the SLAC hybrid facility. The rapid cycling bubble chamber is the cylinder shown in a cut-away drawing of its magnet body. Steel hadron filters used in the K^- exposure are shown in front of S4 and S5. The beam is incident from the left foreground.

Fig. 2. Momentum resolution versus momentum of the fast forward track a) as measured using the bubble chamber only and b) after requiring a hybrid fit to the bubble chamber measurements and the PWC data.

Fig. 3. Distribution of missing mass squared (MM^2) calculated with unfitted quantities for events giving fully constrained kinematic fits to reactions 3 and 4.

Fig. 4. Detection efficiency for reaction 3. Note the change of scale at $t = -.20$ GeV^2.

Fig. 5. Dalitz plots of $K^+\pi^+$ or $\pi^-\pi^+$ versus $\Lambda\pi^+$ for reactions 3 and 4.

Fig. 6. Momentum transfer squared versus the square of the $\Lambda\pi^+$ mass for reactions 3 and 4.

Fig. 7. Distribution of the $\Lambda\pi^+$ invariant mass. The solid line represents the result of the maximum likelihood fit.

Fig. 8. Decay angular distributions of the Y*(1385) produced in reaction $\pi^+p \to K^+\pi^+\Lambda$ with $m_{\Lambda\pi^+} < 1.55$ GeV/c^2: θ and ϕ are polar angles of the Λ in the $\Lambda\pi^+$ rest frame and θ' and ϕ' are polar angles of the decay proton in the Λ rest frame. The solid lines are results of the maximum liklihood fit.

Fig. 9. Differential cross sections of the Y*(1385). The lines are results of fits to reaction 1 (solid line) and to reaction 2 (dashed line).

Fig. 10. Absolute values of the Y*(1385) transversity amplitudes. The dashed lines are prediction of the Stodolsky-Sakurai and the additive quark models.

Fig. 11. Helicity density matrix elements of the Y*(1385). The dashed lines are predictions of the Stodolsky-Sakurai and the additive quark models.

Fig. 12. Momentum dependence of Σ^+ production cross section at two fixed values of momentum transfer. Data points come from ref. [2, 5, 16-19].

Fig. 13. Momentum dependence of the integrated cross section for Y*(1385) production. Data points come from ref. [2-4, 17].

Fig. 14. Momentum dependence of Y*(1385) production cross section at two fixed values of momentum transfer. Data points come from ref. [2-4, 17, 18].

SLAC HYBRID FACILITY

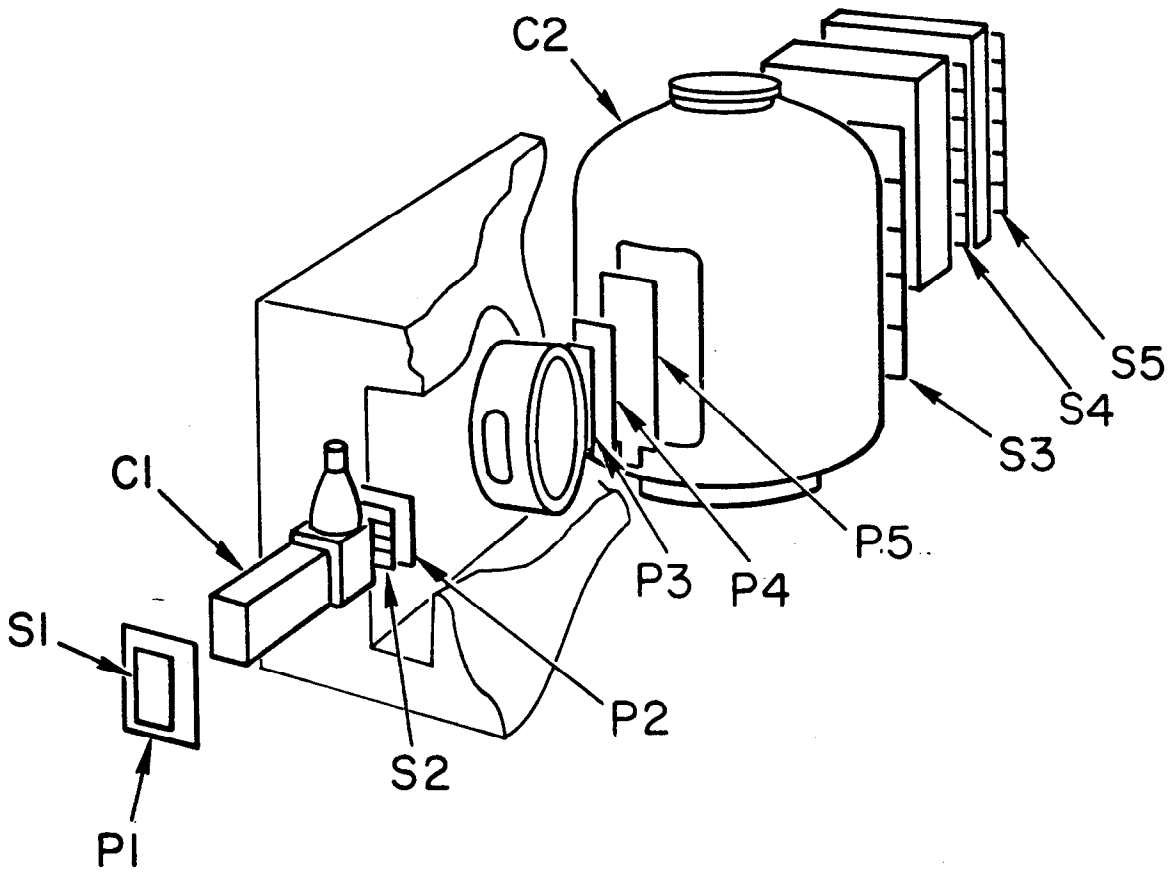

S1 Beam Scintillator
S2-5 Hodoscopes
C1-2 Cerenkov Counters
P1-5 P.W.C.s

9-78

3460A7

Fig. 1

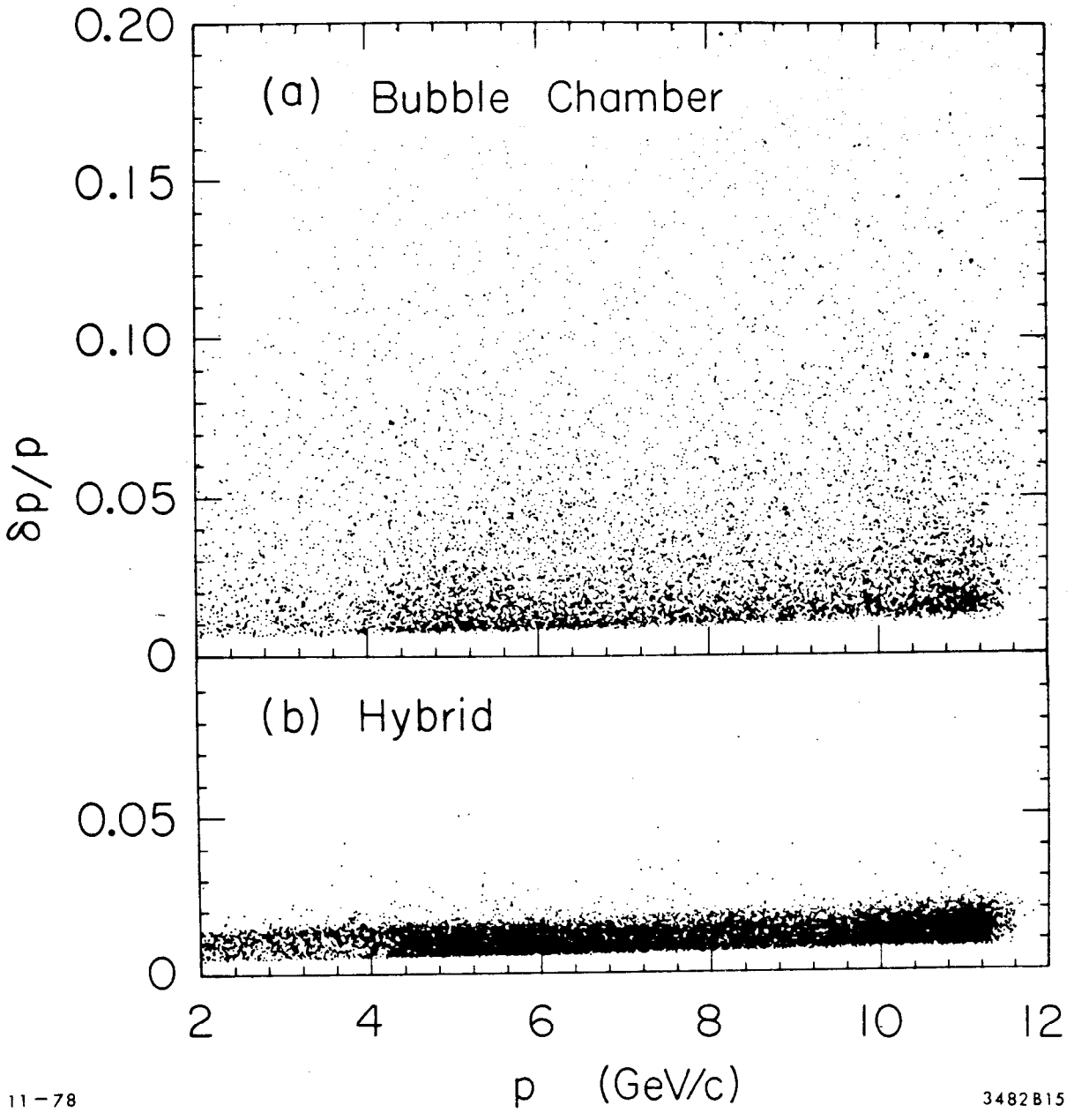
0.20
0.15
0.10
0.05
0
(a) Bubble Chamber
(b) Hybrid
0.05
0
δp/p
2
4
6
8
10
12
p (GeV/c)
11-78
3482B15

Fig. 2

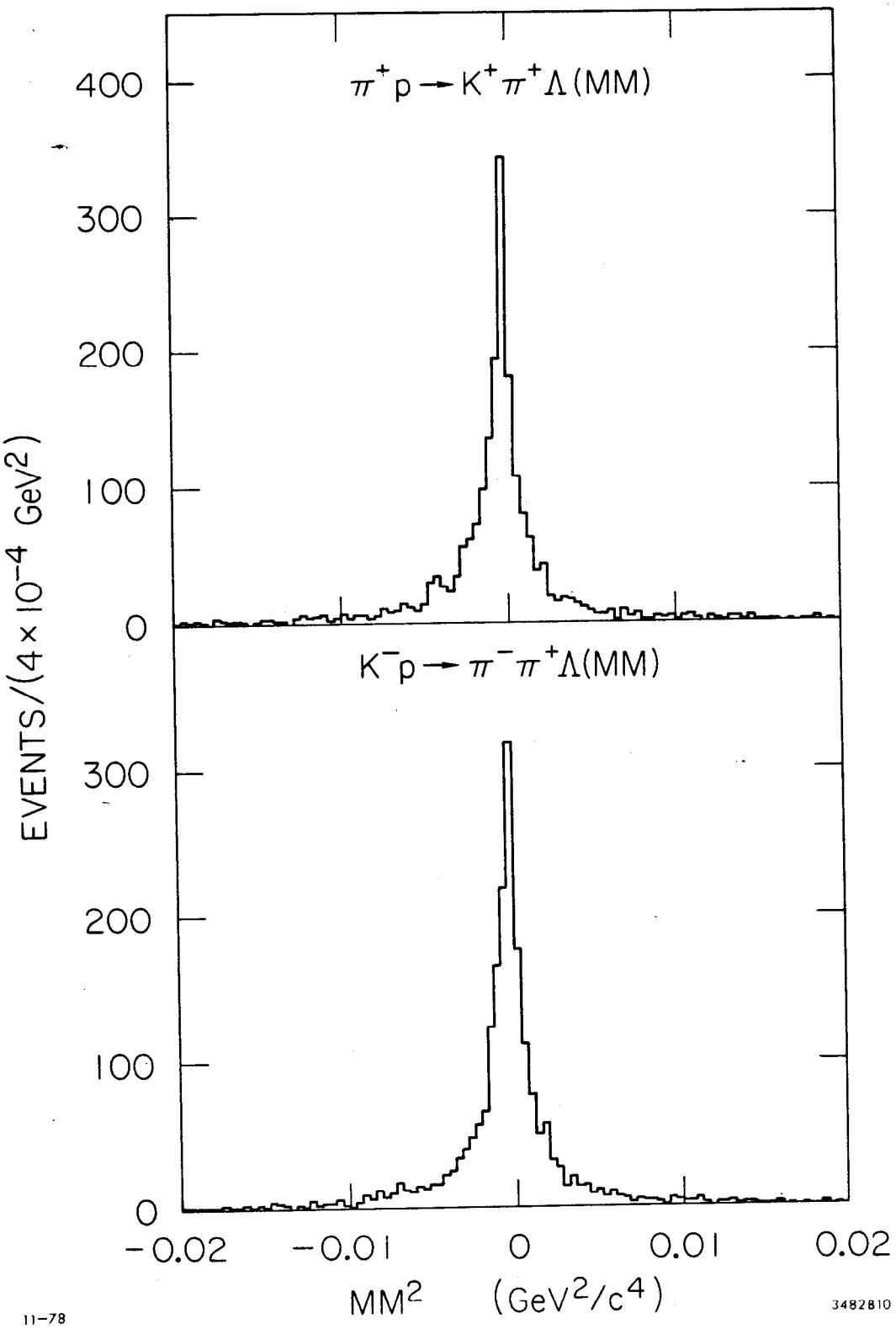
$\pi^+ p \rightarrow K^+ \pi^+ \Lambda$(MM)
$K^- p \rightarrow \pi^- \pi^+ \Lambda$(MM)
EVENTS/(4 × 10^{-4} GeV^2)
400
300
200
100
0
300
200
100
0
−0.02
−0.01
0
0.01
0.02
MM^2 (GeV^2/c^4)
11-78
3482810

Fig. 3

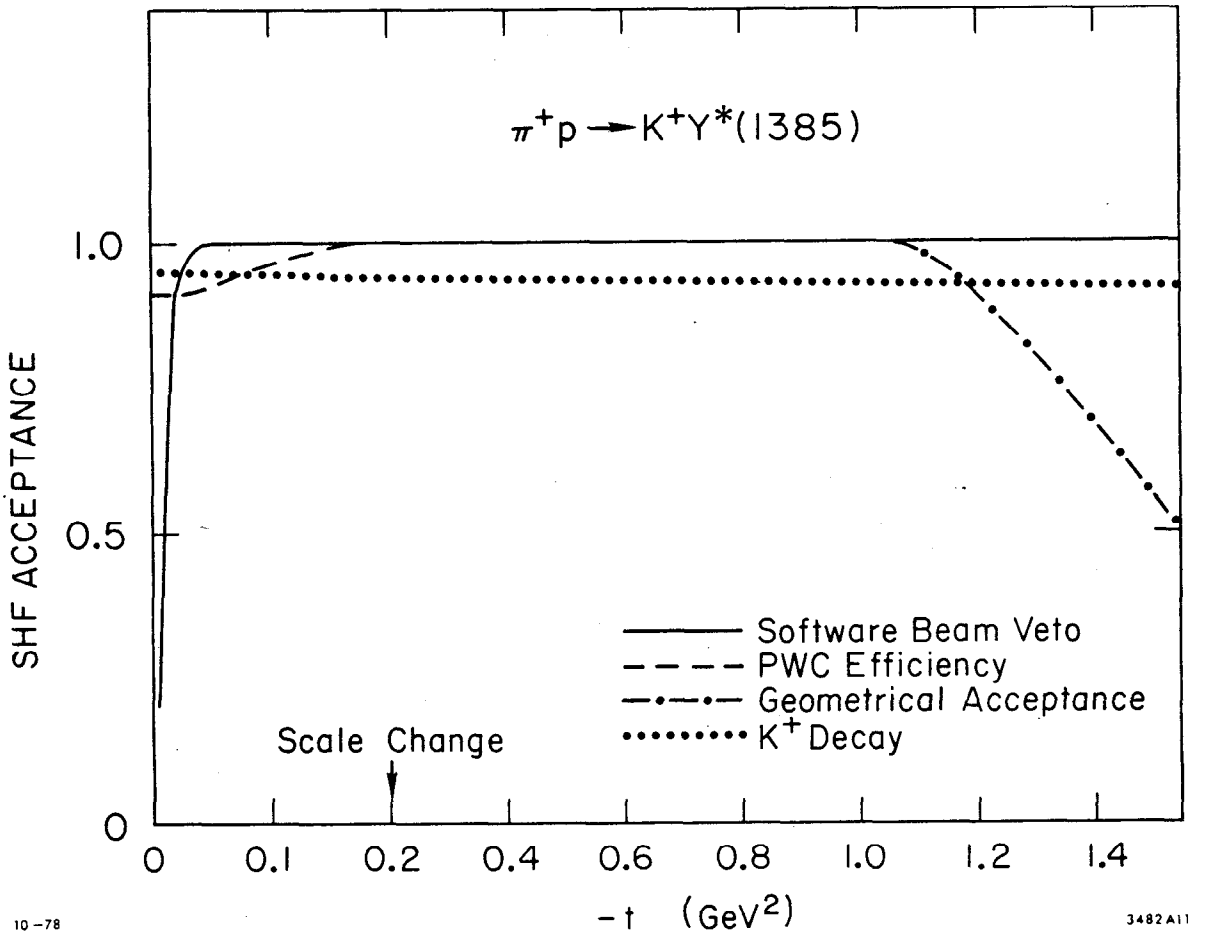
$\pi^+ p \rightarrow K^+ Y^*(1385)$
SHF ACCEPTANCE
1.0
0.5
0
Software Beam Veto
PWC Efficiency
Geometrical Acceptance
K^+ Decay
Scale Change
0
0.1
0.2
0.4
0.6
0.8
1.0
1.2
1.4
$-t$ (GeV^2)
10-78
3482A11

Fig. 4

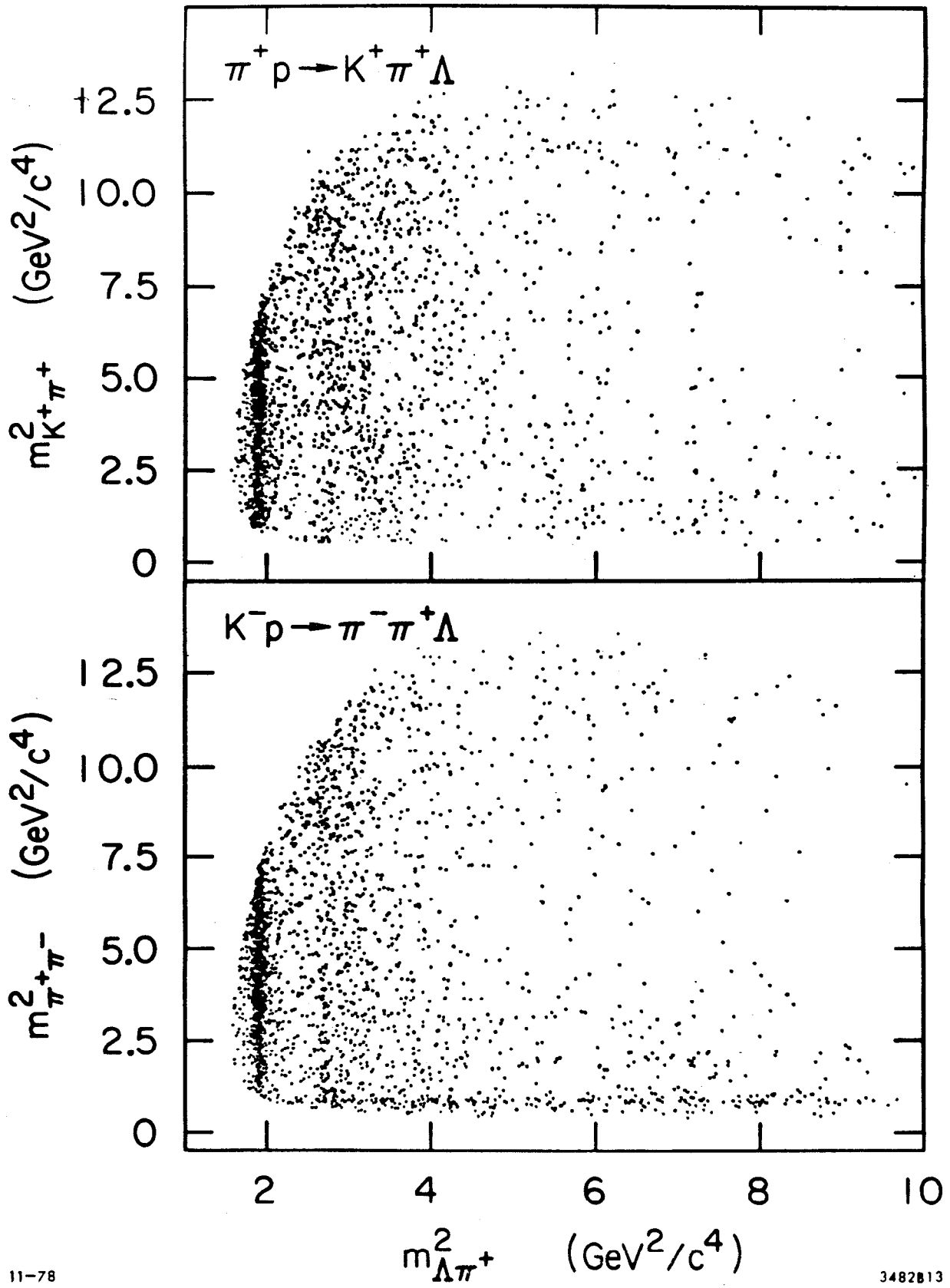
$\pi^+ p \rightarrow K^+ \pi^+ \Lambda$
$K^- p \rightarrow \pi^- \pi^+ \Lambda$
$m^2_{K^+\pi^+}$ (GeV^2/c^4)
$m^2_{\pi^+\pi^-}$ (GeV^2/c^4)
$m^2_{\Lambda\pi^+}$ (GeV^2/c^4)
12.5
10.0
7.5
5.0
2.5
0
2
4
6
8
10
11-78
3482813

Fig. 5

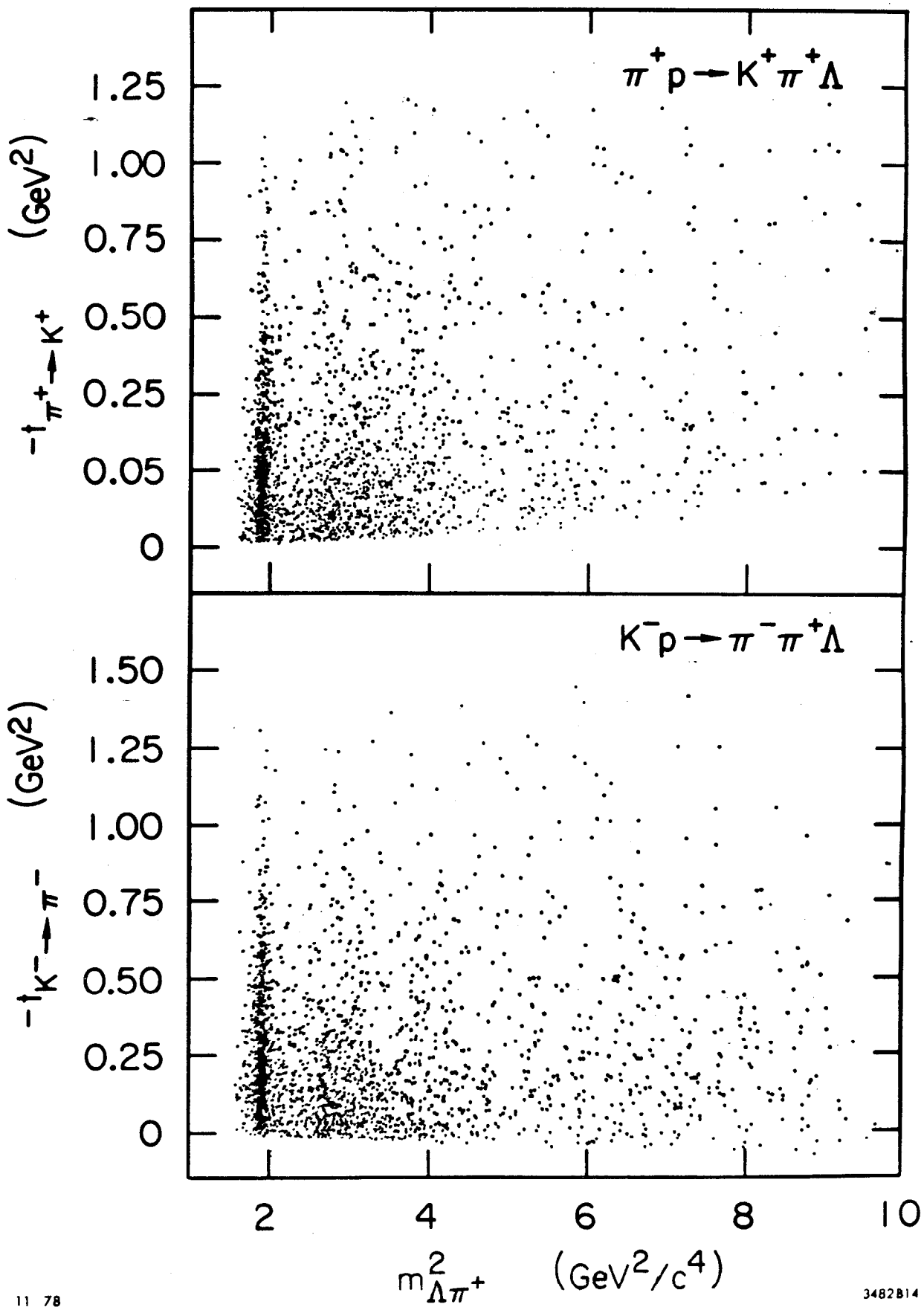
$\pi^+ p \to K^+ \pi^+ \Lambda$
$K^- p \to \pi^- \pi^+ \Lambda$
$-t_{\pi^+ \to K^+}$ (GeV^2)
$-t_{K^- \to \pi^-}$ (GeV^2)
1.25
1.00
0.75
0.50
0.25
0.05
0
1.50
1.25
1.00
0.75
0.50
0.25
0
2
4
6
8
10
$m^2_{\Lambda\pi^+}$ (GeV^2/c^4)
11 78
3482B14

Fig. 6

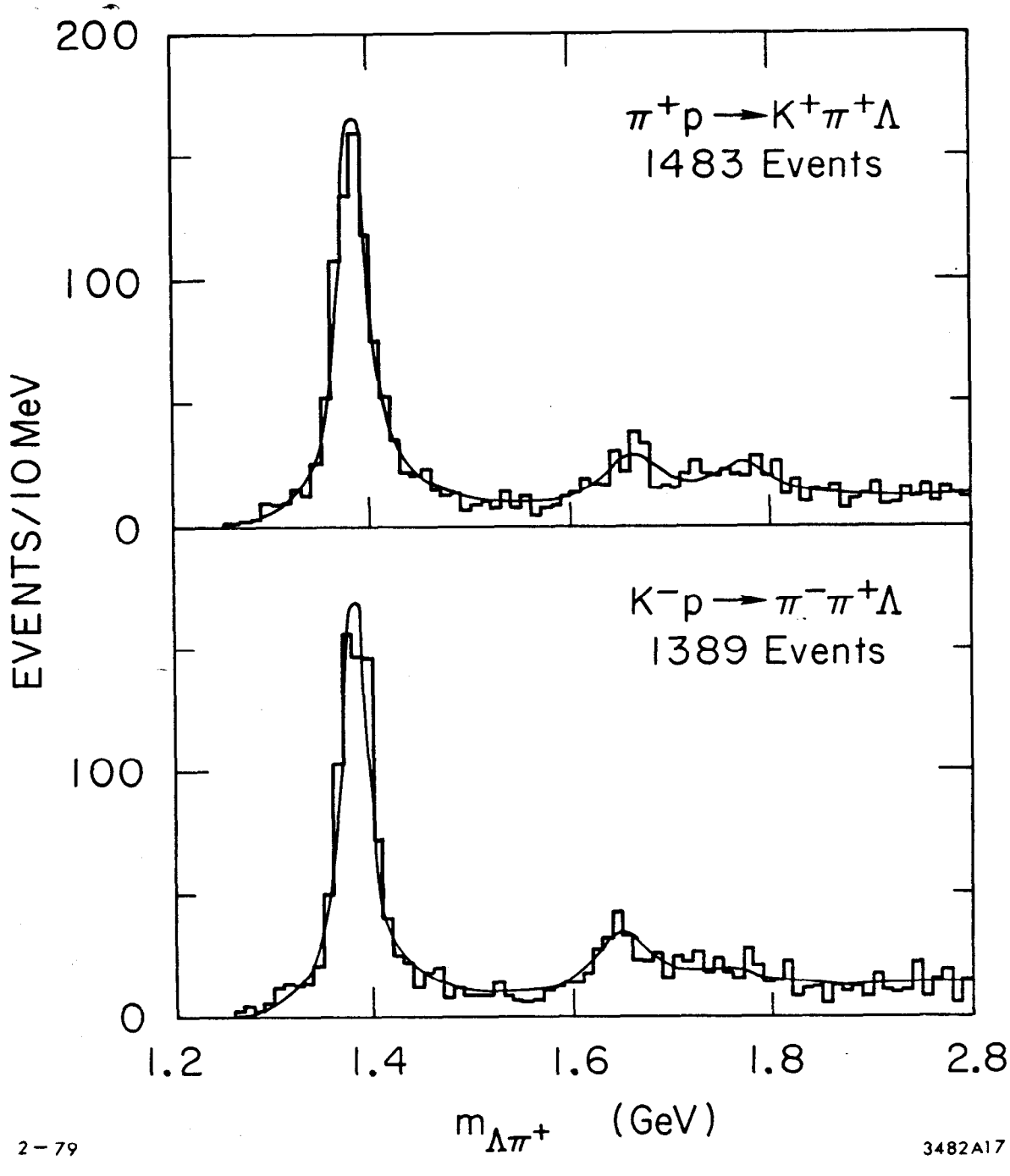
200
100
0
EVENTS/10 MeV
$\pi^+ p \rightarrow K^+ \pi^+ \Lambda$
1483 Events
$K^- p \rightarrow \pi^- \pi^+ \Lambda$
1389 Events
100
0
1.2
1.4
1.6
1.8
2.8
$m_{\Lambda\pi^+}$ (GeV)
2-79
3482A17

Fig. 7

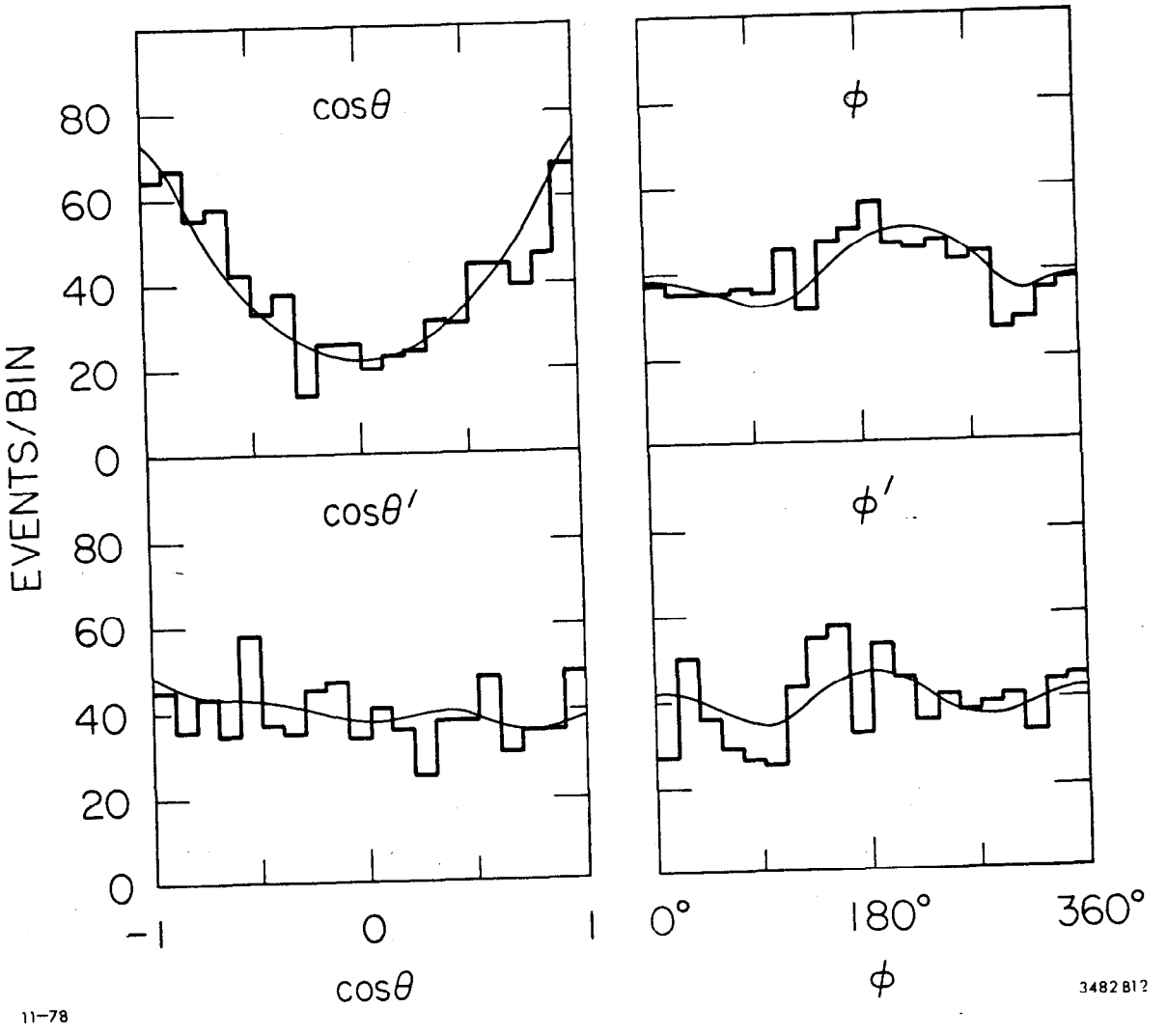
cosθ
φ
cosθ′
φ′
EVENTS/BIN
80
60
40
20
0
−1
0
1
0°
180°
360°
cosθ
φ
11-78
3482B12

Fig. 8

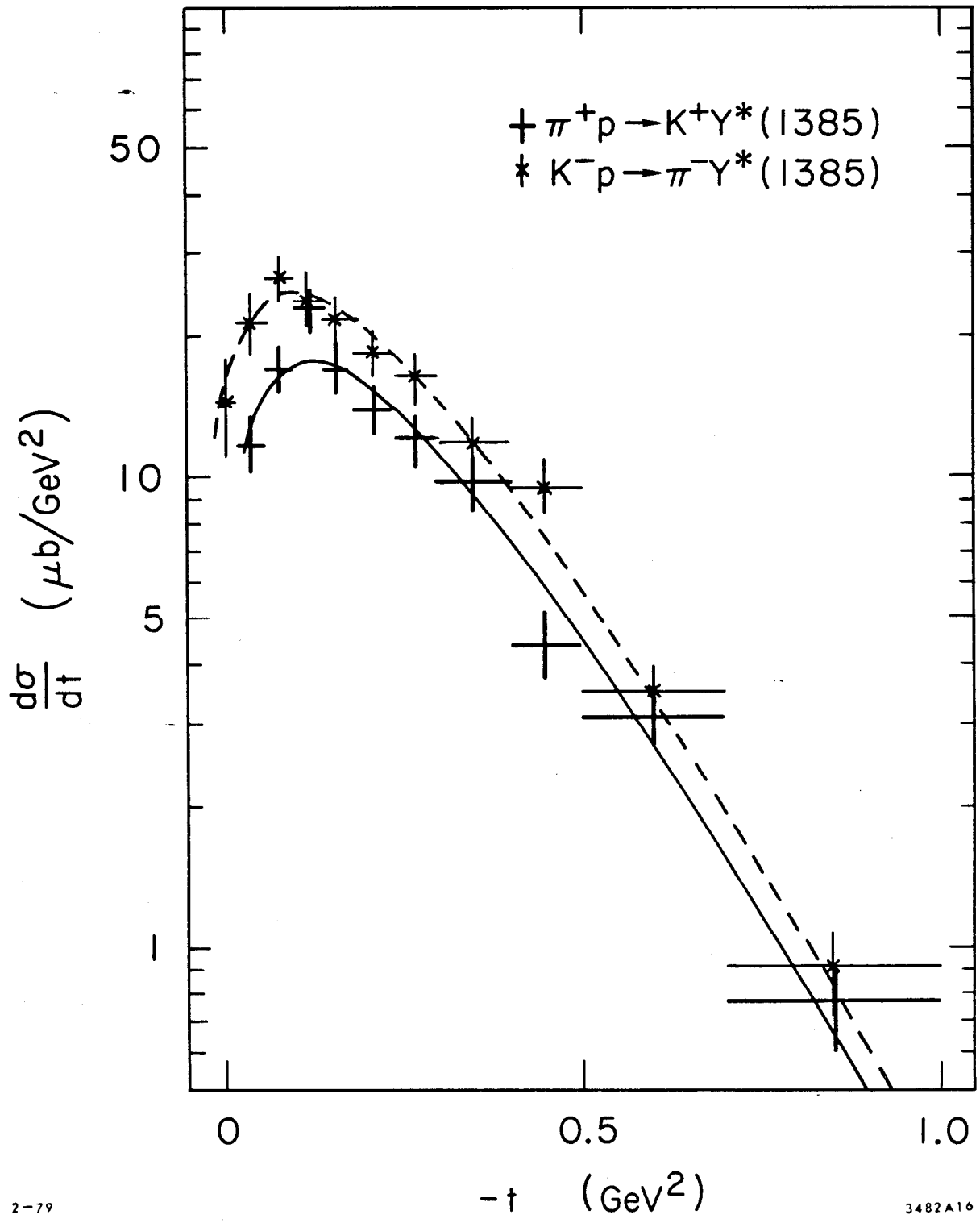
+ π⁺p → K⁺Y*(1385)
* K⁻p → π⁻Y*(1385)
50
10
5
1
dσ/dt (μb/GeV²)
0
0.5
1.0
-t (GeV²)
2-79
3482A16

Fig. 9

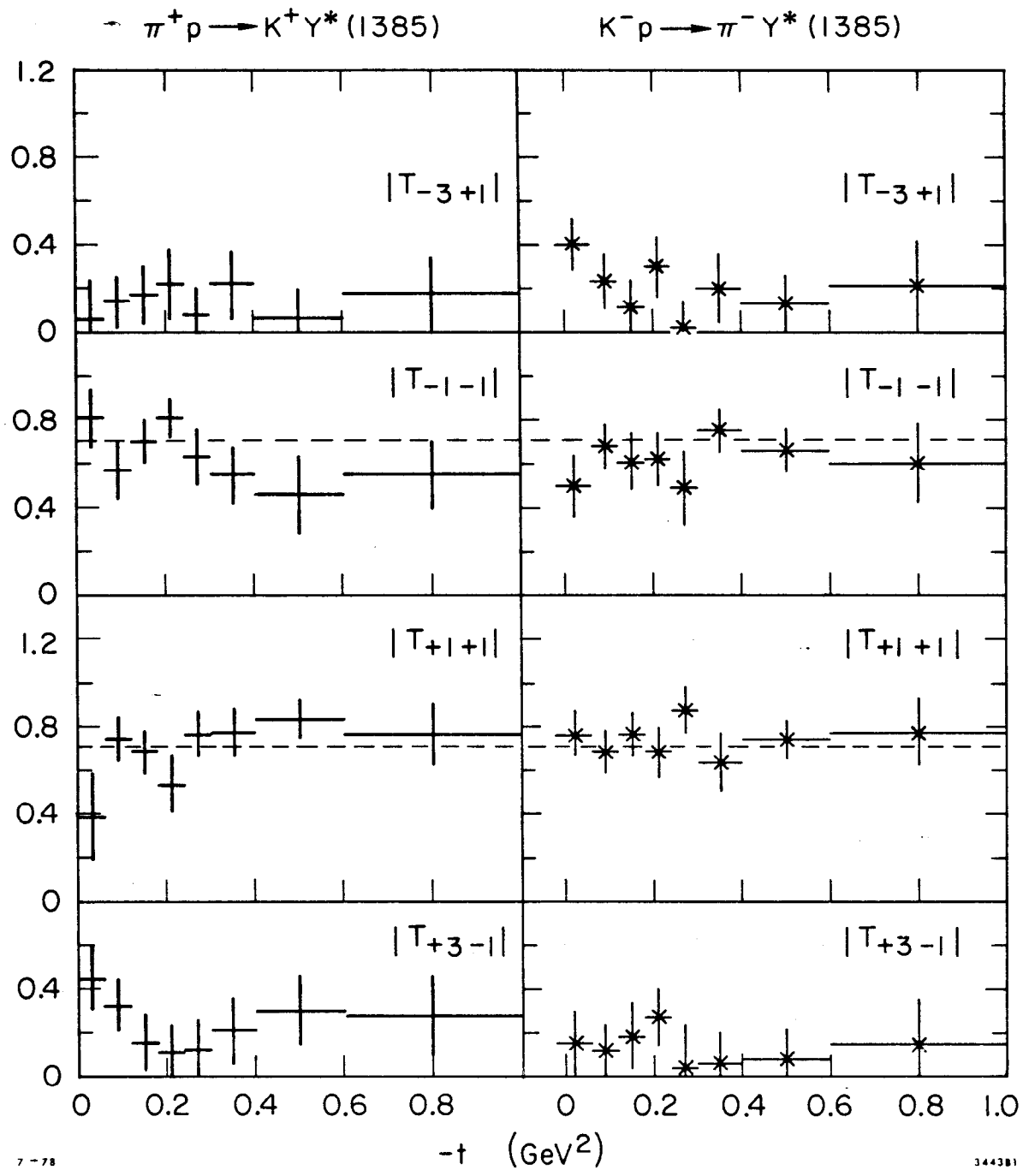
$\pi^+ p \rightarrow K^+ Y^*(1385)$
$K^- p \rightarrow \pi^- Y^*(1385)$
$|T_{-3+1}|$
$|T_{-1-1}|$
$|T_{+1+1}|$
$|T_{+3-1}|$
1.2
0.8
0.4
0
0.2
0.6
1.0
$-t$ (GeV^2)
7-78
344381

Fig. 10

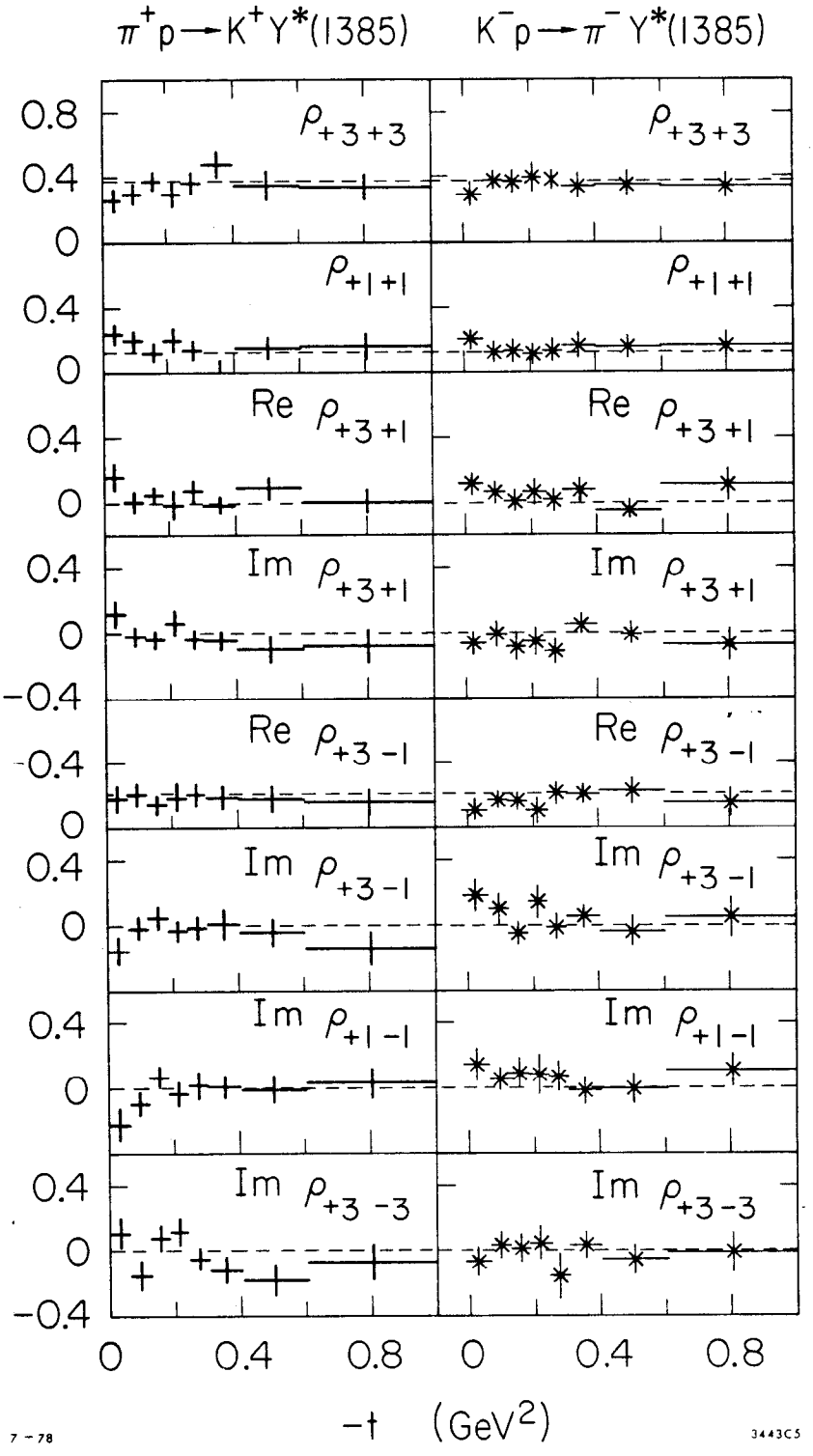
$\pi^+ p \to K^+ Y^*(1385)$
$K^- p \to \pi^- Y^*(1385)$
ρ_{+3+3}
ρ_{+1+1}
Re ρ_{+3+1}
Im ρ_{+3+1}
Re ρ_{+3-1}
Im ρ_{+3-1}
Im ρ_{+1-1}
Im ρ_{+3-3}
0.8
0.4
0
-0.4
0
0.4
0.8
$-t$ (GeV^2)
7-78
3443C5

Fig. 11

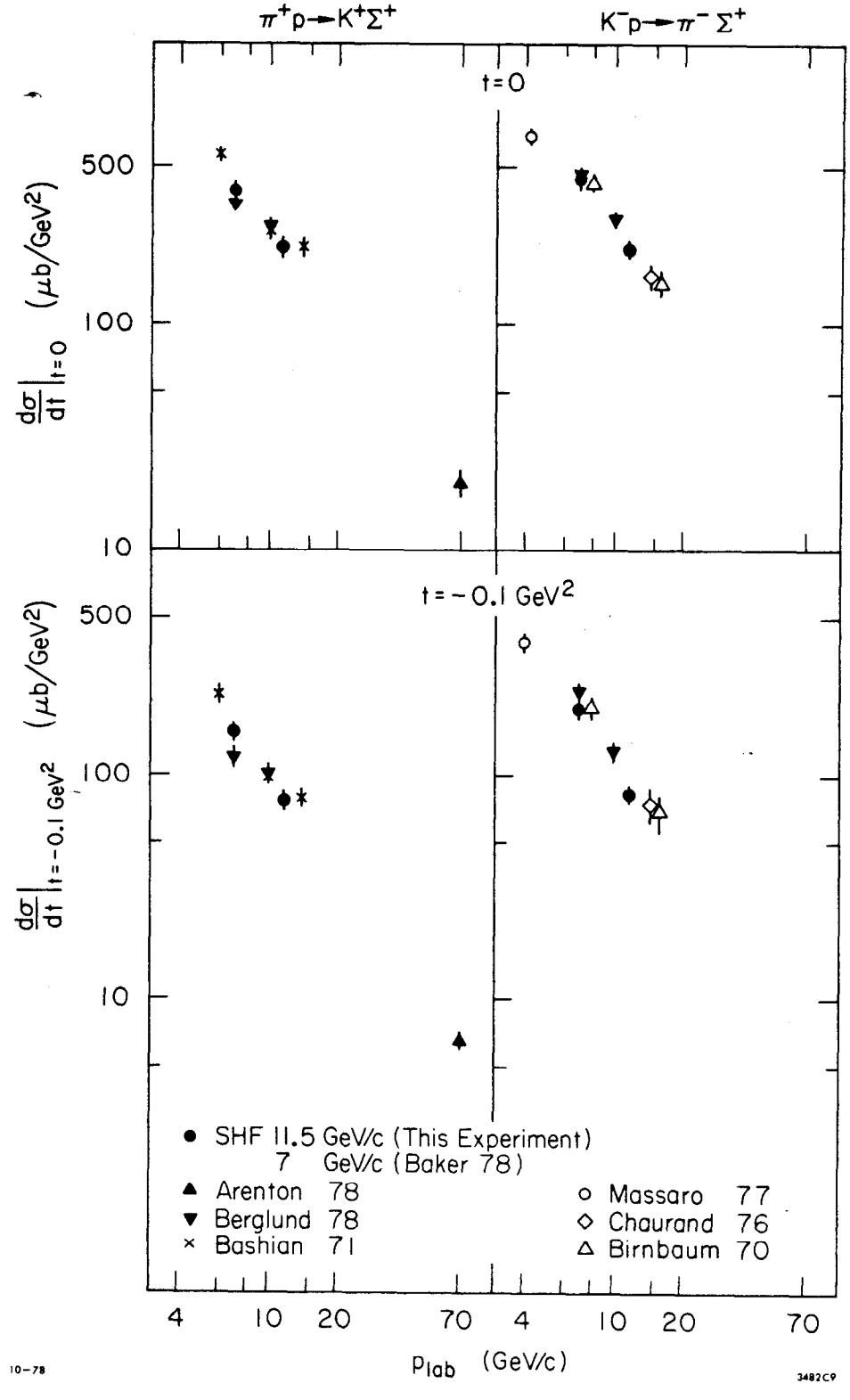
$\pi^+p \to K^+\Sigma^+$
$K^-p \to \pi^-\Sigma^+$
t=0
$t=-0.1\ GeV^2$
$\frac{d\sigma}{dt}\Big|_{t=0}$ ($\mu b/GeV^2$)
$\frac{d\sigma}{dt}\Big|_{t=-0.1\ GeV^2}$ ($\mu b/GeV^2$)
500
100
10
4
10
20
70
p_{lab} (GeV/c)
SHF 11.5 GeV/c (This Experiment)
7 GeV/c (Baker 78)
Arenton 78
Berglund 78
Bashian 71
Massaro 77
Chaurand 76
Birnbaum 70
10-78
3482C9

Fig. 12

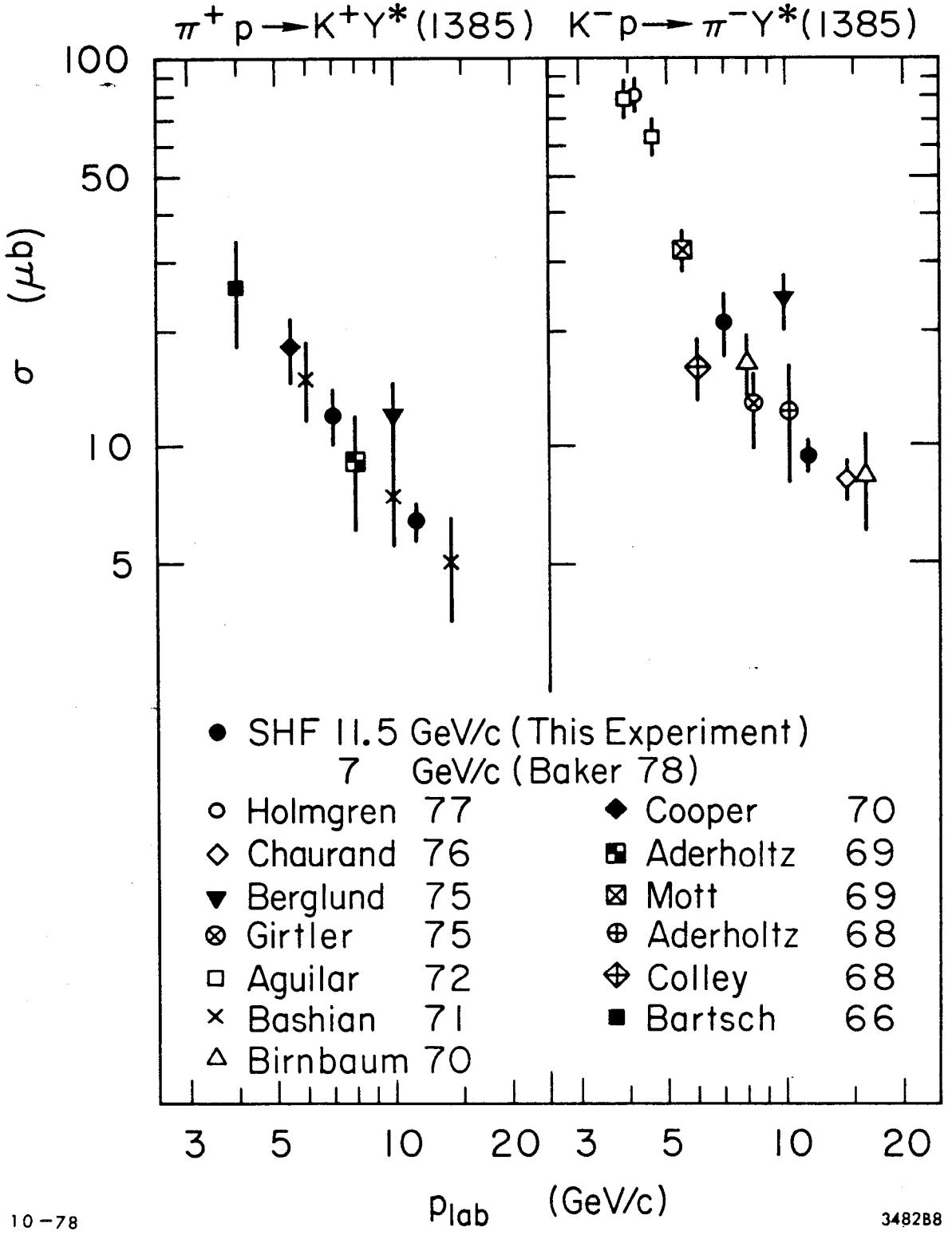
$\pi^+ p \rightarrow K^+ Y^*(1385)$
$K^- p \rightarrow \pi^- Y^*(1385)$
100
50
10
5
σ (μb)
● SHF 11.5 GeV/c (This Experiment)
7 GeV/c (Baker 78)
○ Holmgren 77
◇ Chaurand 76
▼ Berglund 75
⊗ Girtler 75
□ Aguilar 72
× Bashian 71
△ Birnbaum 70
◆ Cooper 70
▪ Aderholtz 69
⊠ Mott 69
⊕ Aderholtz 68
⊕ Colley 68
■ Bartsch 66
3 5 10 20 3 5 10 20
p_{lab} (GeV/c)
10-78
348288

Fig. 13

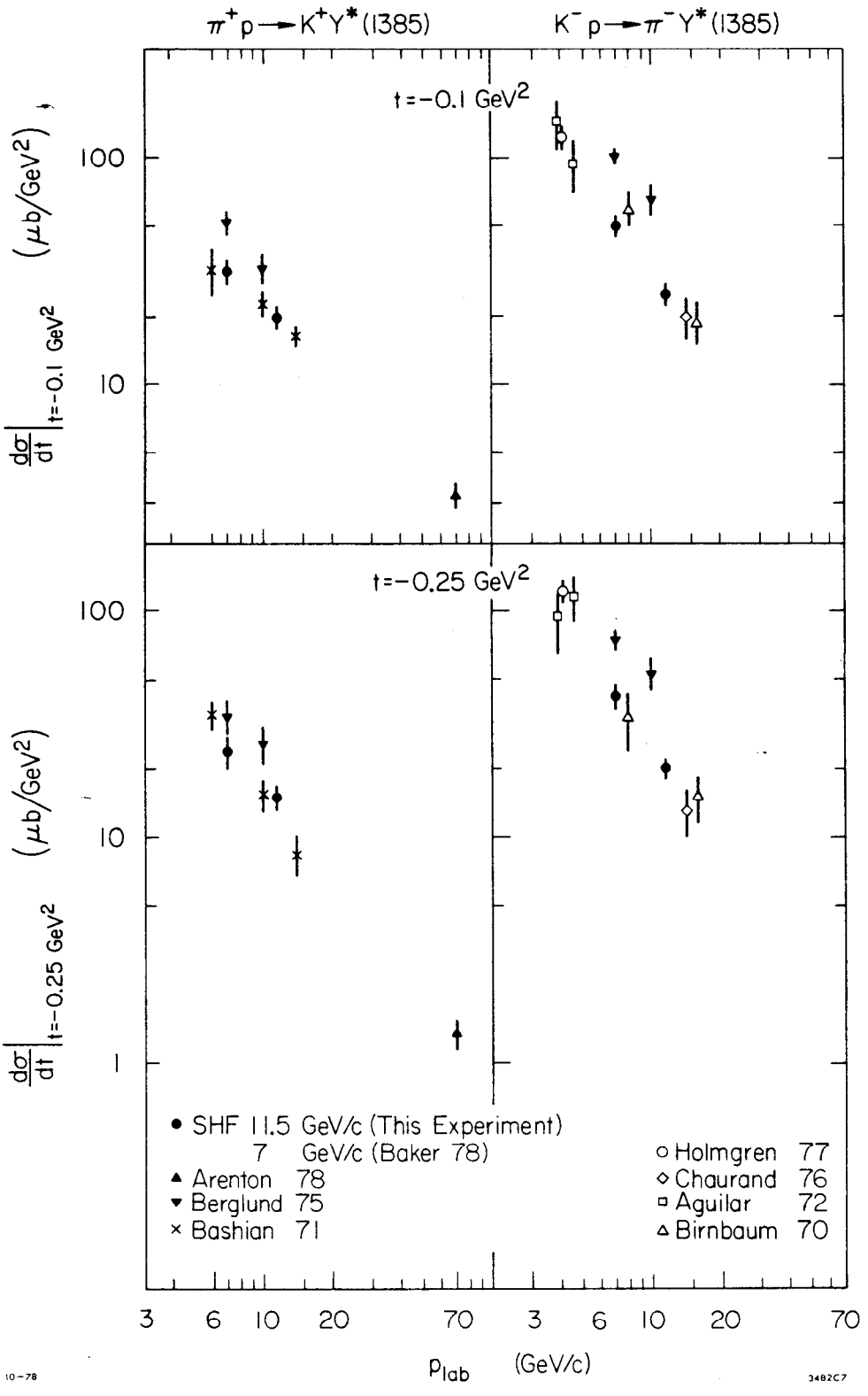
$\pi^+ p \rightarrow K^+ Y^*(1385)$
$K^- p \rightarrow \pi^- Y^*(1385)$
t=-0.1 GeV^2
t=-0.25 GeV^2
$\frac{d\sigma}{dt}\Big|_{t=-0.1\ GeV^2}$ (μb/GeV^2)
$\frac{d\sigma}{dt}\Big|_{t=-0.25\ GeV^2}$ (μb/GeV^2)
100
10
1
3
6
10
20
70
p_{lab} (GeV/c)
• SHF 11.5 GeV/c (This Experiment)
7 GeV/c (Baker 78)
▲ Arenton 78
▼ Berglund 75
× Bashian 71
○ Holmgren 77
◇ Chaurand 76
□ Aguilar 72
△ Birnbaum 70
10-78
3482C7

Fig. 14